Summer 8-23-2019

Development of an Electrical Interface for A Lateral Field Excited Sensor System

Thomas J. Leighton
thomas.leighton@maine.edu

DEVELOPMENT OF AN ELECTRICAL INTERFACE FOR A LATERAL FIELD EXCITED SENSOR SYSTEM

By

Thomas J. Leighton

B.S. University of Maine, 2017

A THESIS

Submitted in Partial Fulfillment of the

Requirements for the Degree of

Master of Science

(in Electrical Engineering)

The Graduate School

The University of Maine

May 2019

Advisory Committee:

Nuri Emanetoglu, Associate Professor of Electrical and Computer Engineering, Advisor

John Vetelino, Professor of Electrical and Computer Engineering

Mauricio Pereira da Cunha, Professor of Electrical and Computer Engineering

DEVELOPMENT OF AN ELECTRICAL INTERFACE FOR A LATERAL FIELD EXCITED SENSOR SYSTEM

By Thomas J. Leighton

THESIS Advisor: Dr. Nuri Emanetoglu

An Abstract of the THESIS Presented
in Partial Fulfillment of the Requirements for the
Degree of Master of Science
(in Electrical Engineering)
May 2019

Sensor systems are utilized to provide critical information to an end user which may range from a physician in a heath care facility to a soldier in a battle field environment. The "heart" of the sensor system is the sensing platform, examples of which include semiconductor, piezoelectric and optical devices. The responses of these sensors must be converted into a format that the user can read and interpret. This conversion is achieved through integrating the sensing platform with an electrical interface.

The focus of this thesis is the development of the first electrical interface for Quartz Crystal Microbalance (QCM) sensors in the Lateral Field Excitation (LFE) configuration. Common techniques used for interfacing with thickness field excitation (TFE) QCM devices include impedance-based systems, oscillator systems, and phase-mass based systems. Although oscillators have been successfully designed for TFE QCMs, attempts to develop an oscillator-based interface system for the LFE QCMs operating in air and vacuum media have been unsuccessful. A comparative study of LFE and TFE sensors operating in air and vacuum media was

conducted to determine the reason why these interfaces do not work with LFE QCMs. It was concluded that compared to TFE sensors LFE sensors have higher motional resistance, R_m, and narrower separation between the series and parallel resonant frequencies, which inhibited oscillation. To identify an optimum configuration for the 6MHz LFE sensor based on the sensor's impedance response, 45 different configurations for the LFE sensor were fabricated and tested.

Based on the conclusions of the comparative study and further investigation into QCM electrical interfaces, two electrical interface systems were investigated for the chosen LFE: the Balanced Bridge Oscillator (BBO) and the Phase Shift Monitoring system. The BBO, a type of frequency tracking system, was selected as the parallel capacitance seen by the sensor can be compensated for, improving the bandwidth of the sensors impedance response. This circuit can be tuned to match the LFE response, and incorporate automatic gain control. However, The fabricated BBO was unable to achieve a stable oscillation with current LFE devices.

The Phase-Shift Monitoring system, which is based on the Phase-Mass characterization method, utilizes an external signal to excite the sensor, and the change in the phase shift of the sensor is tracked as a load is applied to it. The system outputs two DC signals corresponding to the detected change in phase-shift and signal amplitude. The Phase-Mass Monitoring system was tested using both liquid and solid loading with the LFE sensor, and was able to consistently detect masses in the 10s of micrograms range. When the LFE was loaded with $52\mu g$ in air, the system output 7.45mV with a tolerance of $\pm$0.6mV.

The Phase-Shift Monitoring system is the first electrical interface to be successfully integrated with the LFE sensor platform in air and vacuum media, where oscillator-based systems have been unsuccessful. Further work and testing on the system are required to fully characterize the phase-mass relationship of the LFE, as well as developing the system for commercialization.

ACKNOWLEDGEMENTS

I would like to first thank Nuri Emanetoglu for the opportunity of having his mentorship throughout my undergraduate and graduate career. I would like to thanks Jequil Hartz for his crucial role in this project. Additionally I would like the extend my gratitude and appreciation the other members of my advisory committee; John Vetelino, and Mauricio Pereira da Cunha. I also owe thanks to my electrical engineering professors, particularly Duane Hanselman for his mentorship and advice throughout my time at the University of Maine. I must also thank Andrew Sheaff and Nicholas Aiken for their technical input and expertise, guidance, and wisdom throughout the duration of this project. And finally, I would like to express my gratitude for all of the support and encouragement provided by my family; I would not be where I am today without them. Without the assistance of all of those mentioned, completion of a Master's Degree in Electrical Engineering at the University of Maine would not have been possible.

TABLE OF CONTENTS

LIST OF TABLES

LIST OF FIGURES

CHAPTER 1
INTRODUCTION

1.1 Background

A Quartz Crystal Microbalance (QCM) is a device that can measure mechanical changes on the sensing surface of the device, such as changes in mass, density, and viscoelasticity variations[1]. To measure these variations the changes in the sensing platform's impedance response, series resonant frequency, or phase-shift at a constant frequency[2] are tracked. To use the QCM, it must be integrated with an electrical interface. This interface allows the user to measure and detect changes in the QCM's response, as well as to apply an electric field to excite the sensor. Electrical interfaces that are used commercially vary in complexity, cost, accuracy and portability.

There are two types of configurations for the QCM, Thickness Field Excitation (TFE) and Lateral Field Excitation (LFE). The TFE configuration has electrodes on opposite surfaces to excite the QCM through its thickness. The LFE configuration leaves the sensing surface bare by having both electrodes on one surface to excite the QCM parallel to the surface[3]. The TFE configuration has proven to be a reliable and easy to implement sensor. The LFE configuration has the advantage of detecting both mechanical and electrical property changes due to the fact that the sensing side of the device is bare[4]. The TFE configuration has been used since the 1980s, while the LFE sensor configuration has only been investigated since the early 2000s. Due to this, all current designs for an electrical interface for the QCM sensing platform are for the TFE sensors[5], and no designs have been successfully adapted for current iterations of the LFE sensors operating in air or vacuum media.

1.2   Purpose and Objectives

The purpose of this thesis was to investigate, develop, and test an electrical interface for LFE sensor systems operating in air or vacuum environments. Furthermore, this thesis also sought to identify an optimum LFE electrode configuration by investigating the dependence of the admittance response on the electrode configuration, surface curvature, and electrode separation. The Butterworth Van Dyke (BVD) equivalent lumped-circuit model parameters were extracted to analyze device behavior and to design electrical interface circuits. The BVD equivalent circuit, which is commonly used for modeling TFE devices[5], was selected as a model of the LFE. The target sensor applications are air and vacuum media, and this model has been shown to be accurate for the LFE sensor operating in these media[6].

45 different LFE configurations were fabricated and the admittance response for each configuration was measured by Jequil Hartz[7]. The BVD model parameters for the fabricated sensors were derived from the measured admittance responses. These models for the fabricated 6MHz LFE devices were then compared to the BVD model for a 6MHz TFE device. The optimum LFE configuration was identified using these data.

To develop a compatible and effective electrical interface for the LFE, the existing systems for QCM sensors were reviewed. Where previous work on interfacing the LFE sensor with a conventional oscillator-based frequency tracking system have failed, a comparative study was done on three of these systems to determine why these designs work for the TFE and not the LFE. The systems investigated were the Clapp, Miller and Pierce oscillator systems [8, 9, 10].

The Balanced Bridge oscillator [11] system was also investigated, simulated, constructed and tested. The phase-mass method[12], an alternative to the frequency tracking method, was also investigated. This Phase-Shift Monitoring system was

designed, simulated, constructed and tested for the LFE sensor platform. This system is the first system to successfully be integrated with the LFE sensor platform for mass sensing in air and vacuum media.

1.3 Organization

This thesis is organized into five chapters. The Introduction provides background on the LFE and TFE sensing platforms, as well as the electrical interfaces investigated in this thesis. This chapter also describes the purpose and objectives of this thesis, and presents the organization of this thesis.

The second chapter provides theoretical background on the QCM, covering both TFE and LFE configurations for the QCM. The Butterworth Van Dyke lumped-circuit equivalent model, and how it explains the sensors performance is discussed. This chapter also provides an overview of several electrical interfaces used in QCM monitoring and those investigated in this thesis.

The third chapter describes the process of identifying optimum LFE device configuration parameters. The variations on LFE configurations were electrode diameter, electrode separation and surface curvature. For each of these configurations, the Butterworth Van Dyke equivalent models were derived. This chapter also provides and analysis and discussion of the results, identifying the LFE configuration which is optimum for sensor systems and electrical interfacing.

The fourth chapter provides a description of the electrical interface systems investigated in this research. The simulation, experimental setup, and method for testing the developed LFE electrical interface systems are discussed. These interfaces include the Clapp oscillator, the Miller oscillator, the Pierce oscillator, the Balanced Bridge oscillator and the Phase-Shift Monitoring systems. The investigated systems were tested with both TFE and LFE sensors. Finally, this chapter presents and discusses the final simulation and experimental results found

for each system and showing that the Phase-Shift Monitoring system is the first interface to successfully be integrated with the LFE sensor platform in air and vacuum media.

The fifth chapter provides a summary of the completed work, discusses the conclusions found in the thesis, and describes the future work that should be performed for the LFE interface.

CHAPTER 2
BACKGROUND

This chapter provides background on the QCM sensor platform and both the TFE and LFE configurations. The Butterworth Van Dyke model for these sensor platforms is discussed. This model is used to design the electrical interfaces investigated in this research and used to identify an optimum LFE sensor configuration. The background on the electrical interfaces investigated in this research are presented in this chapter.

2.1 The Basic Principles of AT-Cut Quartz Resonators

The QCM sensor platform uses an AC electrical signal that is applied to electrodes on the device, in both the TFE or LFE configurations, to excite bulk acoustic waves (BAW). A standing wave is generated in the QCM when the thickness of the QCM is an odd multiple of half the wavelength of the excited acoustic wave. The BAW sensor can be excited in three excitation modes: the longitudinal mode, the fast shear mode, and the slow shear mode. The Longitudinal mode has displacements collinear with the wave propagation direction. The Shear modes have displacements that are perpendicular to the wave propagation direction [13]. Each of the modes have a corresponding velocity, where the longitudinal mode has the highest velocity and the slow shear mode has the slowest. The thickness of the QCM and the excitation mode determines the operating frequency of the device.

One of the most widely used substrates in QCM devices is AT-cut quartz as it allows for coupling to a purely slow shear mode. AT-cut quartz is also temperature compensated around room temperature, meaning that the frequency changes due to temperature changes is minimized. AT-cut quartz was selected for LFE device

fabrication in this investigation. Other materials, such as Lithium Tantalate ($LiTaO_3$), have been tested and found to be viable alternatives[14].

As mass is deposited onto the QCM, the series resonant frequency of the sensor will decrease due to mass loading. This change in frequency can be detected using an electrical interface with the QCM, by tracking the series resonance frequency, the phase-shift at a constant excitation frequency, or measuring the frequency dependent impedance response of the QCM.

2.1.1   The Piezoelectric Effect

Piezoelectricity is the phenomenon in which an electric charge is generated in noncentrosymmetric crystals, such as quartz, in response to a mechanical stress that is applied to the material. The discovery of the piezoelectric effect was inspired by the discovery of the pyroelectric effect by Carl Linnaeus and Franz Aepinus in mid 1700s [15]. A pyroelectric material generates an electrical potential in response to temperature changes. The brothers Pierre Curie and Jacques Curie would draw from the pyroelectric effect to demonstrate the piezoelectric effect in 1890 [16].

The piezoelectric effect is the result of electromechanical interactions between the electrical and mechanical states in materials that are acentric [17], that is, those that crystallize in noncentrosymmetric space groups. A mechanical stress applied to a noncentrosymmetric crystal results in a shift of the location of atoms which causes the dipoles of the crystal to shift, generating an electric field. When the stress is applied in the correct orientation of the crystal (excitation mode), a change will occur in the net dipole moment, producing a change in the electrical field on the crystal.

Materials that exhibit the piezoelectric effect are also subject to the reverse piezoelectric effect, which is the generation of mechanical strain as the result of an applied electrical charge. This effect is the basis for crystal resonators [18]. The

6

inverse piezoelectric effect is represented in AT-cut quartz resonator in Figure
2.1[19].
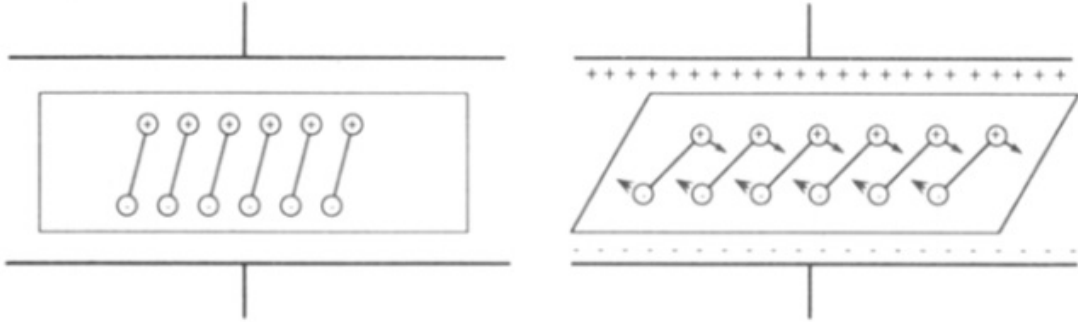
Figure 2.1. Representation of inverse piezoelectric effect for shear motion.

2.1.2 Thickness and Lateral Field Excitation

TFE sensor platforms require the AT-cut quartz to have electrodes deposited on
opposite faces of the wafer, as shown in Figure 2.2[14].
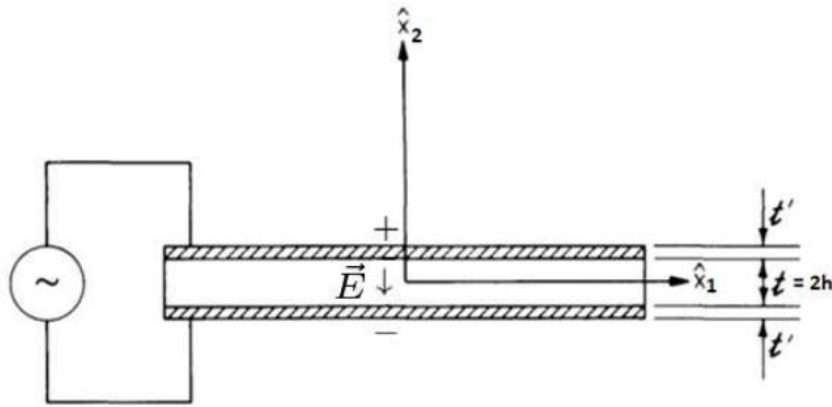
Figure 2.2. Thickness Field Excitation.

Applying a time-varying electric field to the electrodes of the TFE generates a
mechanical vibration, activating the inverse piezoelectric effect. The frequency at
which the TFE resonates is determined by the thickness of the crystal, t, shear
modulus, μ_q, and density, ρ_p. When t is half the acoustical wavelength, a standing

7

wave can be established, where the inverse of the frequency of the applied potential is half of the period of the standing wave.

$$f_o = \frac{\sqrt{\frac{\mu_q}{\rho_q}}}{2t} \qquad (2.1)$$

ρ_p and μ_q for AT-cut quartz are $2.648\frac{g}{cm^3}$ and $2.947\text{x}10^{11}\frac{g}{cms^2}$ respectively. The term $\sqrt{\frac{\mu_q}{\rho_q}}$ in (2.1) can also be simplified to the acoustic velocity, approximately $3332.64\text{x}\frac{m}{s}$ for the slow shear mode in AT-cut quartz. A lateral electric field can also be used to generate an acoustic wave in the AT-cut quartz wafer. This is known as lateral field excitation, LFE. For this configuration electrodes are placed on the same face of the wafer as shown in Figure 2.3[14].
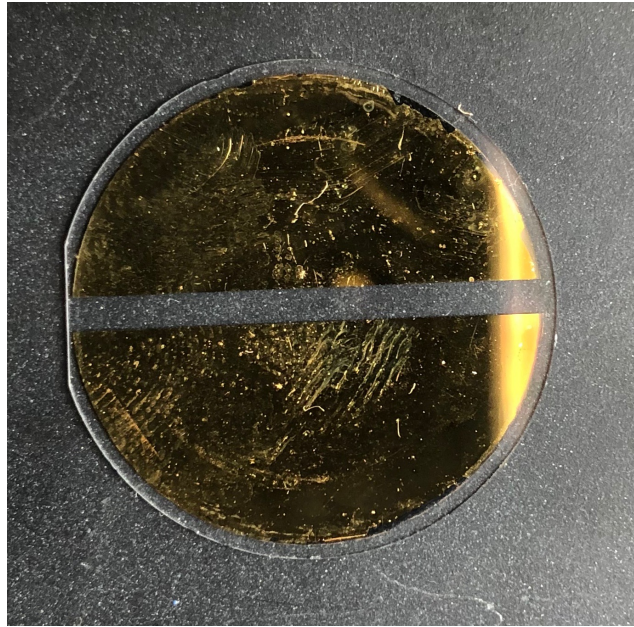
Figure 2.3. Lateral Field Excitation.

The sensing surface of the LFE devices has both electrodes on one surface of the device. This allows LFE devices to be used for sensing both mechanical and electrical changes [20]. The LFE has been proven to be sensitive to mechanical changes like TFE devices [21].

2.1.3   Butterworth Van Dyke Lumped Circuit Model

When the electrical impedance of a crystal resonator is measured and plotted against frequency, as shown in Figure 2.5[22], the response appears similar to a RLC circuit. Therefore, a circuit model can be derived to represent the crystal at the fundamental frequency, as shown in Figure 2.4.
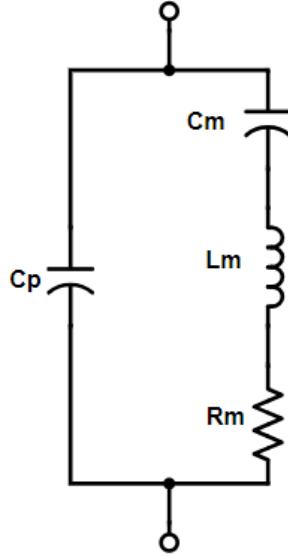
Figure 2.4. Butterworth-Van Dyke equivalent circuit model.

The BVD model in Figure 2.4 shows the circuit equivalent of the resonator near the fundamental resonance or series resonance, where the motional branch of the resonator consists of a series RLC circuit. The motional resistance, R_m, models the energy dissipated during resonance. The motional capacitance, C_m, models the energy stored during resonance. The motional inductance, L_m, models the displaced mass during resonance. The capacitance in the parallel branch, C_p, is the static capacitance of the quartz resonator with electrodes.

The Butterworth-Van Dyke (BVD) model is a suitable lumped circuit model for crystal resonators in air and vacuum media and has been widely used in crystal resonator modeling for both TFE sensing platforms [5, 23]. Additionally, models
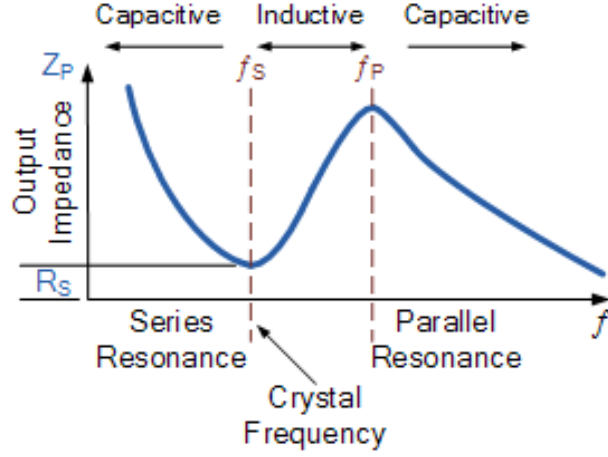
Figure 2.5. Output impedance against frequency of a crystal resonator.

developed for the LFE show that the BVD model works in air and vacuum media at the fundamental frequency[6].

The impedance of a crystal resonator near the resonance frequency can be calculated using the BVD model parameters, and is found to be:

$$Z_{BVD}(s) = \left(\frac{1}{sC_o}\right)\left(\frac{s^2 L_m C_m + s R_m C_m + 1}{s^2 L_m C_m + s R_m C_m + 1\frac{C_m}{C_p}}\right), \tag{2.2}$$

The quality factor, Q, series resonance, f_s, and the parallel resonance, f_p can be calculated using the BVD model parameters:

$$f_s = \frac{1}{2\pi\sqrt{L_m C_m}}, \tag{2.3}$$

$$f_p = \frac{1}{2\pi\sqrt{L_m \frac{C_p C_m}{C_p + C_m}}}. \tag{2.4}$$

$$Q = \frac{f_c}{\Delta f} = \frac{2\pi f_s L_m}{R_m} = \frac{1}{2\pi f_s R_m C_m}, \tag{2.5}$$

10

The center frequency at the midpoint between f_s and f_p is f_c, and δf is the difference between f_s and f_p. By applying (2.5), (2.3), and (2.4) with (2.2), the impedance of the BVD model can be expressed as:

$$Z_{BVD}(s) = \left(\frac{1}{sC_p}\right)\left(\frac{s^2 + s\frac{w_s}{Q} + w_s^2}{s^2 + s\frac{w_s}{Q} + w_p^2}\right), \tag{2.6}$$

where ω is $2\pi f$. The term, $\frac{1}{sC_p}$, which is the impedance of C_p, will be the dominant term in the impedance response of the resonator, as the second term will be close to unity away from the resonant frequencies. When the frequency approaches the series and parallel resonance frequencies, the motional RLC components of the sensor impacts the sensor's response.

2.1.3.1 Ratio of Motional Capacitance and Parallel Capacitance

The ratio between the parallel capacitance, C_p, and the motional capacitance, C_m, of the BVD model for a crystal resonator is referred to as the capacitance ratio, C_r.

$$C_r = \frac{C_p}{C_m} \tag{2.7}$$

Resonators with a larger C_r are inductive for smaller frequency bands, moving the resonant peaks closer together. This also becomes clear when comparing (2.3) and (2.4); as the difference between C_m and C_p becomes larger, increasing C_r, f_p will move closer to f_s. Resonators with a lower C_r, and therefore a larger bandwidth, are desirable for oscillator applications because it allows for efficient external frequency pulling[23].

2.2 Review of QCM Electrical Interface Systems

Several different QCM electronic measurement systems are currently used. The purpose of these systems is to accurately measure the physical variations that

happen while the QCM is being used for sensing applications. These systems vary in cost, level of complexity in design, tuning, accuracy, precision, and portability. Oscillator based and phase-mass based electrical interfaces are investigated for LFE sensors in this thesis. A comprehensive comparison of QCM electrical interfaces is presented in Appendix B.

2.2.1 Oscillator Based Systems

The most common QCM interfaces track the change of f_s using an oscillator circuit. A system must meet the requirements of the Barkhausen criterion to oscillate. According to the Barkhausen criterion the magnitude of the total loop gain must be unity, and the total loop phase-shift must be 0° or multiples of 360° for sustained oscillation at f_s.

The Clapp, Pierce and Miller oscillators are commonly used systems with QCM devices. These systems offer simple and low-cost designs for frequency tracking. However, previous investigations of these oscillator systems [24, 25, 26], have shown that these systems are not compatible with current configurations of the LFE sensor platform operating in air or vacuum media due to the high motional resistance, Q value and C ratio that are related to operating in these media. With these issues in mind, the Balanced Bridge oscillator system was selected for further investigation due to parallel capacitance compensation to help with the C ratio and Q factor.

The Balanced Bridge oscillator, as shown in Figure 2.6, was first proposed to address the additional parasitic parallel capacitance added from the systems connecting cable to the parallel capacitance seen by the sensor [11]. The Balanced Bridge design is used to compensate for the parallel capacitance. The Balanced Bridge oscillator utilizes two equivalent branches with parallel circuit L_c-C_c tanks tuned to reduce the loop-gain for undesired frequencies. A compensation capacitor, C_v, equal to the parallel capacitance of the sensor, is connected to the reference

branch, and the sensor is connected to the other. The output of each branch is connected to an automatic gain control stage, which is tied to the input. The design was further improved in [27], where the transistors were replaced with transconductance amplifiers for improved performance. The design for the balanced bridge oscillator is shown in Figure 2.6.
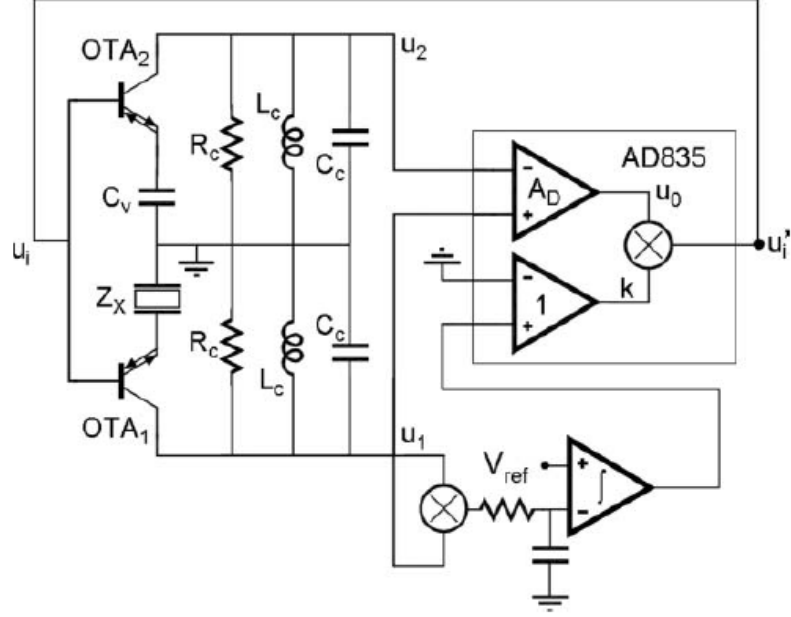
Figure 2.6. Simplified schematic of the balanced bridge oscillator.

The output of the sensor branch and the output of the reference branch are u_1 and u_2 in Figure 2.6 respectively. The input voltage, u_i of the system is transferred to u_1 and u_2 with the following relationships:

$$u1 = u_i Y_x Z_c, \tag{2.8}$$

$$u2 = u_i Y_{C_v} Z_c, \tag{2.9}$$

where Y_x is the admittance of the LFE sensor, Z_x in Figure 2.6, formed by the capacitance in parallel with the impedance of the motional arm of the sensor, Z_m.

13

Z_c is the impedance of the RLC branch of the oscillator, and Y_{C_v} is the admittance of the compensation capacitor. Y_{C_v}, Y_x, Z_c and Z_m can be represented using the following relationships in terms of the angular frequency, ω:

$$Y_{C_v} = j\omega C_v \tag{2.10}$$

$$Y_x = j\omega C_0 + \frac{1}{Z_m} \tag{2.11}$$

$$Z_m = R_m + j(L_m\omega - \frac{1}{C_m\omega}) \tag{2.12}$$

$$Z_c = R_c + j(L_c\omega - \frac{1}{C_c\omega}) \tag{2.13}$$

The difference between the signals u_1 and u_2 is then amplified with a high input impedance differential amplifier (AD835) used for the automatic gain control stage (AGC). The sensor signal u_1 is mixed with itself and the output is low-pass filtered to produce a DC signal. This signal is then used to limit the output, u_i', of the AD835, acting as the AGC for the system.

$$u_i' = u_i A_D k(\frac{1}{Z_m} + j\omega(C_p - C_v))Z_c \tag{2.14}$$

Since u_i' is tied to the input, u_i the loop condition can be simplified to:

$$1 = A_D k(\frac{1}{Z_m} + j\omega(C_p - C_v))Z_c \tag{2.15}$$

Assuming the circuit is oscillating at series resonance, Z_c can be assumed to be R_c, and Z_m is reduced to R_m. Since $C_0 = C_v$, the loop gain can be simplified to:

$$1 = A_D k\frac{R_c}{R_m}, \tag{2.16}$$

14

where k is the automatic gain control signal and A_D is the differential gain. Eq. (2.16) shows that k is proportional the value of R_m and inversely proportional to R_c. The purpose of the AGC is to maintain a constant amplitude for the signal u_1, to achieve stable oscillation.

2.2.2   Phase-Shift Monitoring Systems

An alternate approach to QCM response monitoring is phase-mass characterization. This approach allows for high resolution when frequency shifts are expected to be minimal [27]. This approach uses a reference signal to excite the sensor at a constant frequency. As mass is added to the system, a phase shift in the response of the sensor occurs at the excitation frequency. An expression was developed to link the mass density variations (Δm_c) and surface mass of contacting material (m_L) to the change in the sensors phase-shift ($\Delta \phi$) [28].

$$\Delta \phi \approx -\frac{\Delta m_c}{m_L}, \tag{2.17}$$

The difference between the phase-shift and frequency-shift characterization methods is demonstrated in Figure 2.7[27]. The frequency-shift method tracks the change in the series resonant frequency of the QCM sensor as mass is applied. The phase-shift characterization method uses an external signal to excite the QCM at a set frequency, and mass loading will induce a change in the phase shift of the sensor.
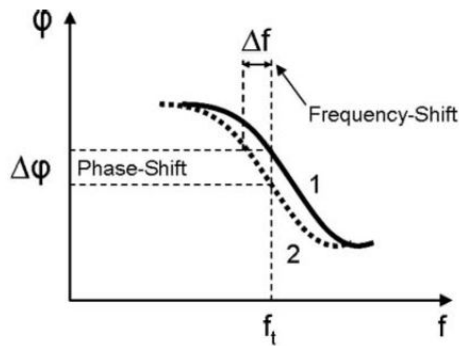
Figure 2.7. Phase-shift characterization vs. frequency-shift.

15

The Phase-Shift Monitoring system described in [12] was investigated and adapted to work with an LFE sensor. The schematic of the Phase-Shift Monitoring system is shown in Figure 2.8. The design has two parallel branches to form a differential circuit, one with the sensor connected and the other with a RC reference circuit. The branches are excited with a constant frequency, f_t, that is close to the unloaded series resonance frequency. This signal is connected to the sensor through a voltage dividing element, R_t. This results in the sensor being the only source for a changing phase-shift.
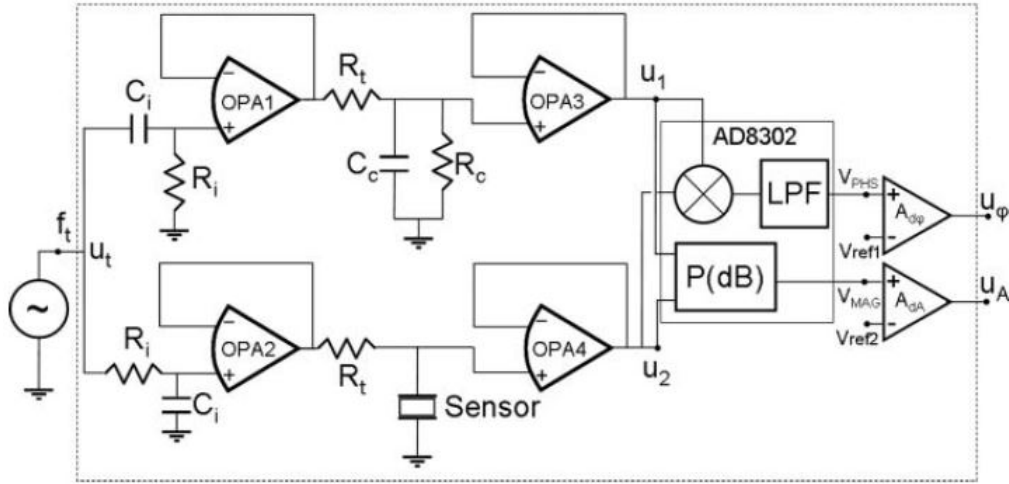
Figure 2.8. Simplified schematic of a phase-shift characterization system.

The characterization system utilizes the AD8302 phase and gain detector from Analog Devices, which has an internal mixer and low pass filter. The phase detector can detect small phase-shifts around 90°. The excitation signal is offset by 90° between the two branches using the R_i and C_i filters, which are tuned to the resonant frequency of the sensor. The gain detector outputs a voltage relative to the u_1/u_2 ratio. The output of the AD8302 is then amplified with the AD623 instrumentation amplifier from Analog Devices to allow for simple centering of the output signals using $V_{ref1,2}$, as well as amplifying the output u_ψ to 100mV$/^o$ and u_A

to 300mV/dB. The operational amplifier OPA656 from Texas instruments was used for the four unity gain buffers.

The RC reference branch R_c and C_c values were set to be equal to R_m and C_p respectively. The resistor R_t and capacitor C_c form a low-pass filter with a high cutoff frequency at the series resonant frequency, R_t is set to be equal to R_c. This results in slow phase noise or jitter being reduced by the differential system, which improves stability.

A calibration method for this system was proposed by Arnau[12]. First the sensor is replaced with R_c-C_c network, forcing the two branches to be identical. The reference voltages $V_{ref1,2}$ can then be adjusted such that u_ψ and u_A are both 0V. Placing the sensor back in, the frequency of u_t is then adjusted such that u_ψ is 0V. An alternative method is discussed in Chapter 4.3. When the sensor is loaded with a mass the phase-shift output signals u1 and u2 can be simplified to the following expression:

$$\Delta(\phi u_1 - \phi u_2) \approx \Delta\phi \frac{R_t}{R_t + R_m}, \tag{2.18}$$

If R_t is set such that it is much larger than R_m, then the resistive part can be reduced to unity. However, to maintain an acceptable output resolution, R_t must not exceed $10R_m$, otherwise the change in the LFE's response becomes negligible compared to R_t[12]. The modifications of the design to operate with an LFE sensor are described in Chapter 4.

CHAPTER 3
LFE MEASUREMENTS AND IMPEDANCE ANALYSIS
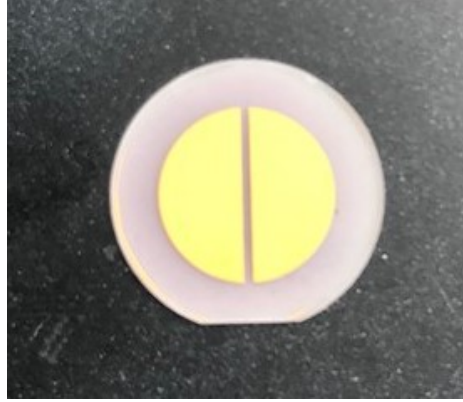
Figure 3.1. Fabricated 6MHz LFE sensor (bottom side).

The narrow bandwidth ($<$100Hz) and low peak-to-peak ($<$25dB) impedance response of the LFE device, as shown in Figure 3.1, provide challenges for developing an electrical interface. To determine an optimum 6MHz LFE configuration to reduce Rm, Cr and improve the impedance response, LFE sensor's response dependence on the following parameters were investigated: sensing surface curvatures, electrode diameter, and electrode separation. The LFE configuration is shown in Figure 3.2.
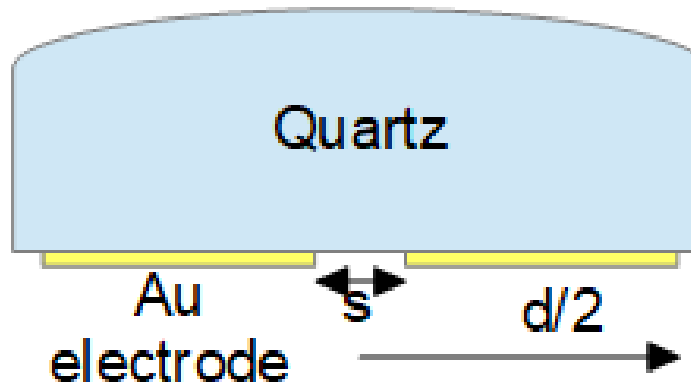
Figure 3.2. Electrode configuration and surface curvature of a LFE.

In Figure 3.2, S is the separation of the electrodes, d is the diameter of the electrodes, and the curvature of the sensing surface is shown. In addition to testing

each configuration with the electrodes directly deposited onto the LFE, further testing was done with the electrodes only on the holder for the sensor, leaving both sides of the QCM devices bare. The fabrication and collection of S11 response for the unloaded LFE devices was done by Jequil Hartz[7]. This data will be used to derive the BVD equivalent model for both analyzing each configuration and component selection for the electrical interfaces investigated.

3.1   Measurement Setup

Once the LFE devices were fabricated, the unloaded impedance response of each device was measured using an E5071C Agilent Technologies Network Analyzer. The devices were measured with a 16KHz bandwidth and an IF bandwidth of 10Hz. The LFE sensors were placed on a FR4 board with the same electrode configuration (if electrodes were deposited on the device). The boards used a 50Ω SMA connector to connect to the network analyzer. Each of the boards were also measured without a device on them so that the admittance response of the boards could be accounted for in the derivation of the BVD model parameter. To investigate if any improvements in the sensors impedance response could be found by exciting the fast shear mode, measurements with the bare LFE devices were made for both the fast shear and slow shear modes.

3.2   Deriving The Butterworth Van Dyke Equivalent Model Parameters

The collected S11 data on the fabricated LFE devices were used to derive the BVD parameters for each device. The S11 data was used to calculate the admittance and impedance response over the measured frequency range.

$$Z = Z_o \frac{1 + S_{11}}{1 - S_{11}} \tag{3.1}$$

$$Y = \frac{1}{Z} \tag{3.2}$$

Once the S11 data were converted into the impedance and admittance data sets, the series and parallel resonance frequencies were found using the local minima and maxima of the admittance magnitude. The motional resistance was calculated using the inverse of the conductance, G, at the series resonance frequency. The parallel capacitance,C_p was determined by the susceptance, B, at the series resonance frequency.

$$Y = G + j * B, \tag{3.3}$$

$$R_m = \frac{1}{G_s}, \tag{3.4}$$

$$C_p = \frac{B_s}{2 * pi * f_s}. \tag{3.5}$$

In (3.4) and (3.5) $G_s$and B_s refer to the conductance and susceptance at the series resonance frequency, as shown in Figure 3.3.

From there, the motional inductance and capacitance by solving (2.3) and (2.4) for C_m and L_m:

$$C_m = C_p \frac{(2\pi f_p)^2}{(2\pi f_s)^2} - C_p, \tag{3.6}$$

$$L_m = \frac{1}{C_m (2\pi f_s)^2}. \tag{3.7}$$

The Q factor can be found using (2.5) from Chapter 2.
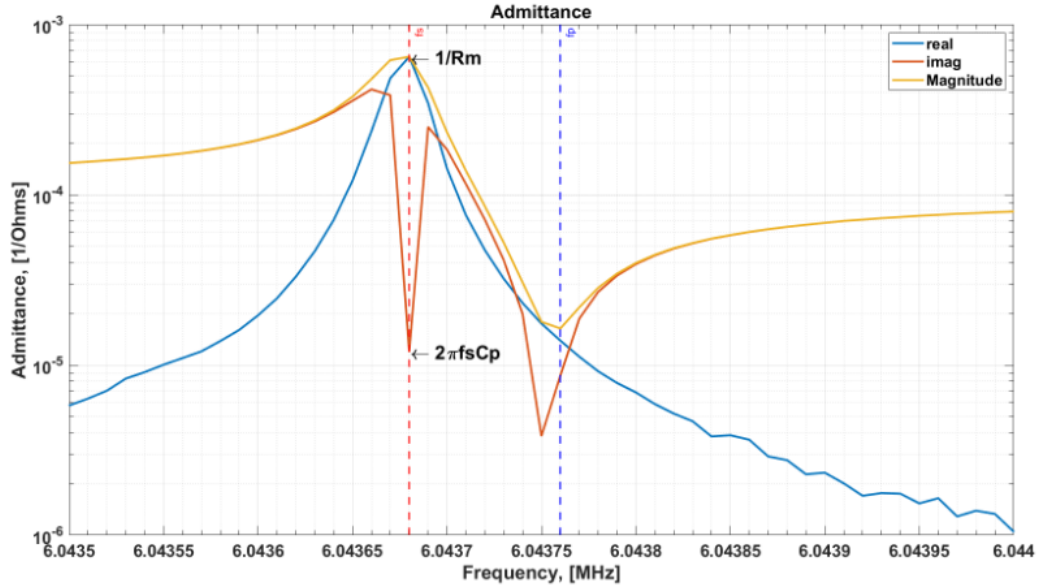
Figure 3.3. Deriving BVD parameters from measured admittance for a LFE sensor.

3.3   Results and Analysis

The data collected from (i) bare quartz samples on patterned PCBs and (ii) LFE devices with electrodes on quartz samples were used to derive BVD parameters. These results were compared to find an optimum LFE curvature and electrode configuration. The optimum device configuration was identified by minimizing the motional resistance and the f_s and f_p separation. The full list of BVD parameters derived for each device is given in Appendix A.

3.3.1   LFE with Deposited Electrodes

To find an optimum LFE device configuration the following device design parameters were varied: the sensing surface curvature was varied from 2 diopter to 6 diopter; the electrode separation was set to 0.5mm, 1.5mm, and 2.5mm; and the diameter of the electrodes were set to 9mm, 11mm, and 13mm.

The derived motional resistance is in the kΩs range for all of the devices, as shown in Figure 3.4. Comparing the results, R_m tends to increase as the separation between the electrodes increases. The motional resistance of the resonator has an

21

inverse relation with the resonant frequency, ω_r, the electric coupling, K^2, and parallel plate capacitance, C_p.

$$R_m = \frac{(\frac{\pi}{2})^2 \alpha}{K^2 \omega_r C_p}. \tag{3.8}$$

In (3.8) α is the absorption value of the material and is approximately $0.0015\frac{1}{m}$ for AT-cut quartz at 6MHz. Measurements have shown that the resonant frequency only varied by 0.019MHz (or $\pm$0.3% of fs). However, variations in C$_p$ and the coupling constant, K, are more significant, $\pm$24.9%, (see Appendix A for C$_p$ data). C$_p$ is determined by the cross sectional area of the QCM and the distance between the electrode plates. Reducing the distance between the electrodes will result in an increased C$_p$ and reduced R$_m$, as is seen in the collected data sets. Therefore these results show that reducing the separation between the electrodes reduces R$_m$ for improved performance.
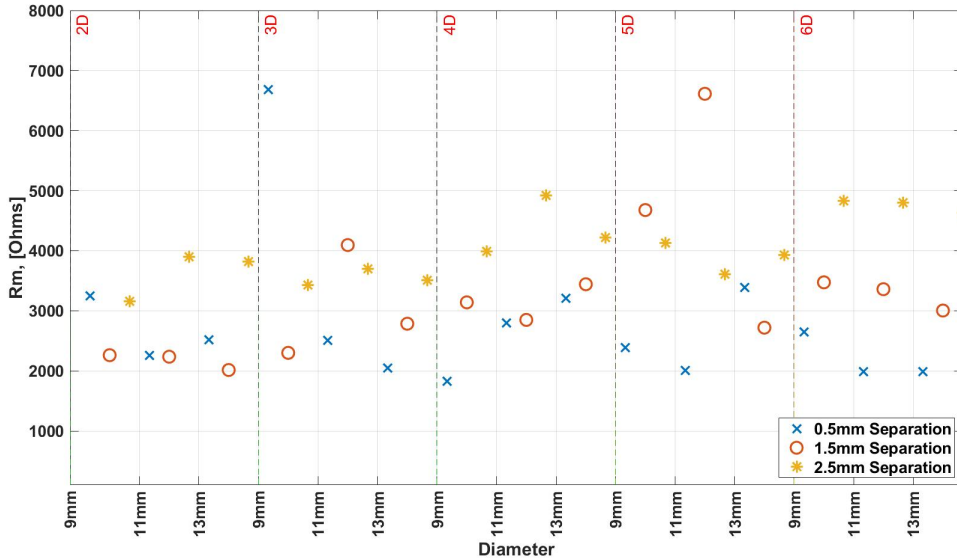
Figure 3.4. Motional resistance of unloaded fabricated LFE devices.

For further improvement of the LFE operation, C$_r$ should be reduced be either increasing C$_m$ and/or decreasing C$_p$ and the bandwidth between f$_s$ and f$_p$ should be

increased. The bandwidth and C_r, shown in Figure 3.5 and Figure 3.6 respectively, show no distinct trends as the electrodes are changed. When looking at only variations in surface curvature, the 2 Diopter samples however, show higher bandwidth with lower C_r.
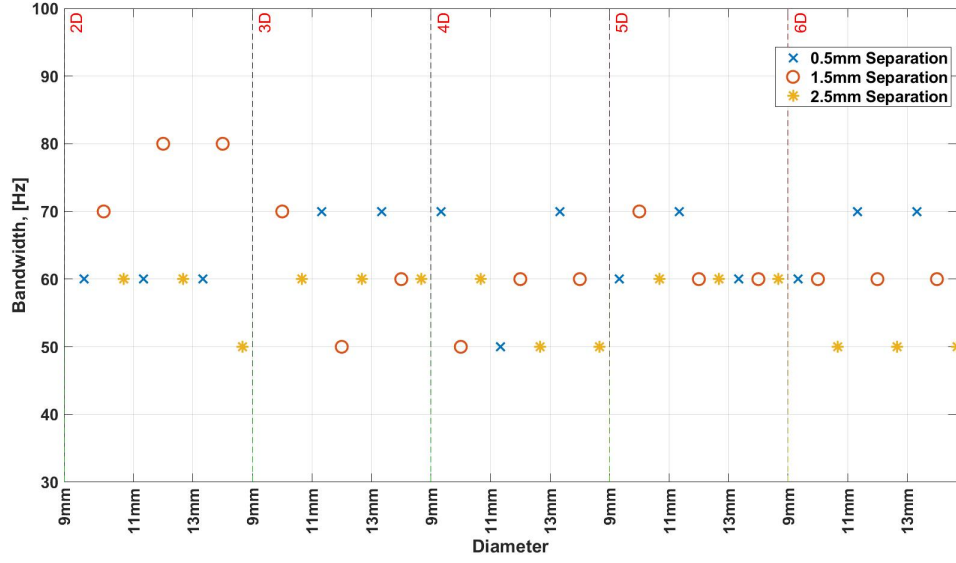
Figure 3.5. Separation between f_s and f_p of unloaded LFE devices.

The measurements of the fabricated LFE devices were done with a 16kHz bandwidth and 1601 data points, resulting in a 10Hz separation consecutive between data points. This presents an issue where most of the LFE devices had a bandwidth under 100Hz, meaning there are under 10 data points of the measured response. In order to improve the accuracy of these results, a narrower measurement, with a smaller bandwidth should be done. However, the currently available data is sufficient for determining an optimum configuration for the LFE.

3.3.2 Bare LFE Samples

Bare LFE samples were tested to compare the impact of deposited electrodes on the quartz sample versus using electrodes patterned on the LFE holder to excite a
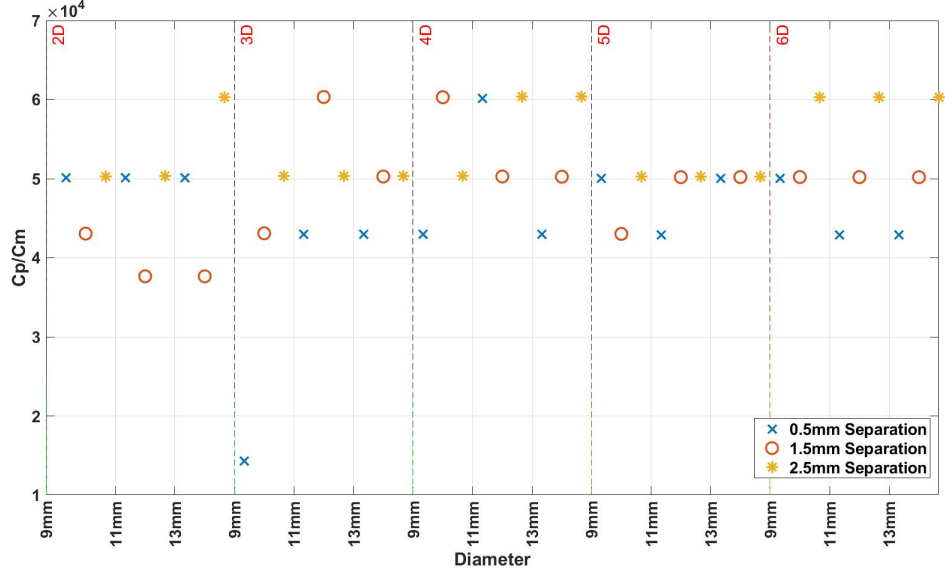
Figure 3.6. Capacitance ratio of unloaded fabricated LFE devices.

bare crystal. By measuring bare samples, Longitudinal and Fast Shear Modes could
be easily measured by rotating the LFE on the holder, without having to fabricate
different devices. The measured impedance response of all three orientations
frequency are shown in Figure 3.7 for a 2 Diopter sample with an electrode
separation of 0.5mm and diameter of 9mm.

The results in Figure 3.7 show the Fast and Slow shear modes preformed
similarly, however the Fast shear has a peak-to-peak response that is greater by
4.1588dB and a bandwidth that is wider by 10Hz than the Slow shear mode
(29.45dB). For further analysis of the LFE devices, the BVD parameters for both
the Fast and Slow shear modes were derived.

3.3.2.1 Slow Shear Mode

Similar to the motional resistance derived for the fabricated LFE samples, the
bare LFE samples, Figure 3.4, also show that R_m decreases with the electrode
separation. Furthermore, R_m increases as the curvature increases. This is likely due
to the cross sectional area of the device decreasing as the surface curvature increases.
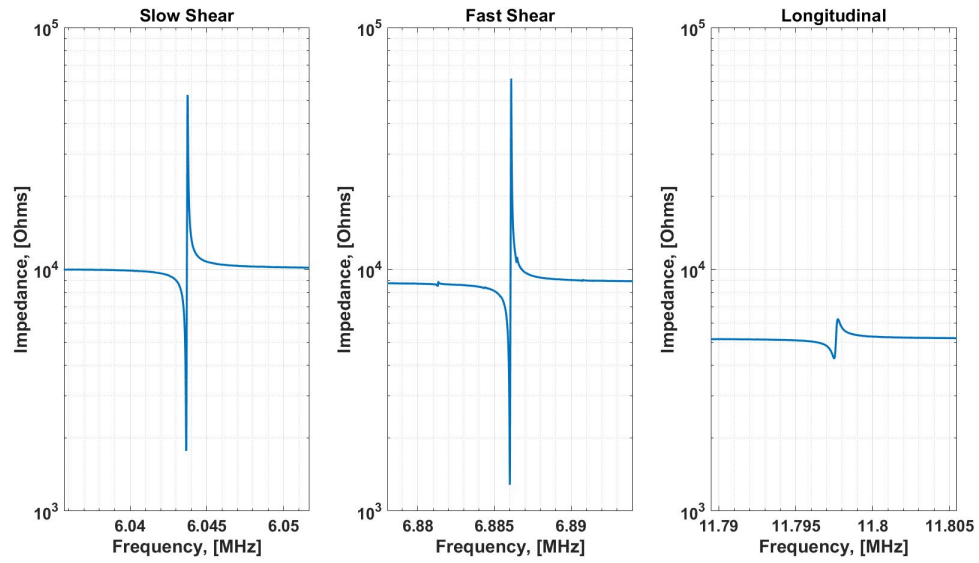
Figure 3.7. Bare unloaded LFE excitation mode.
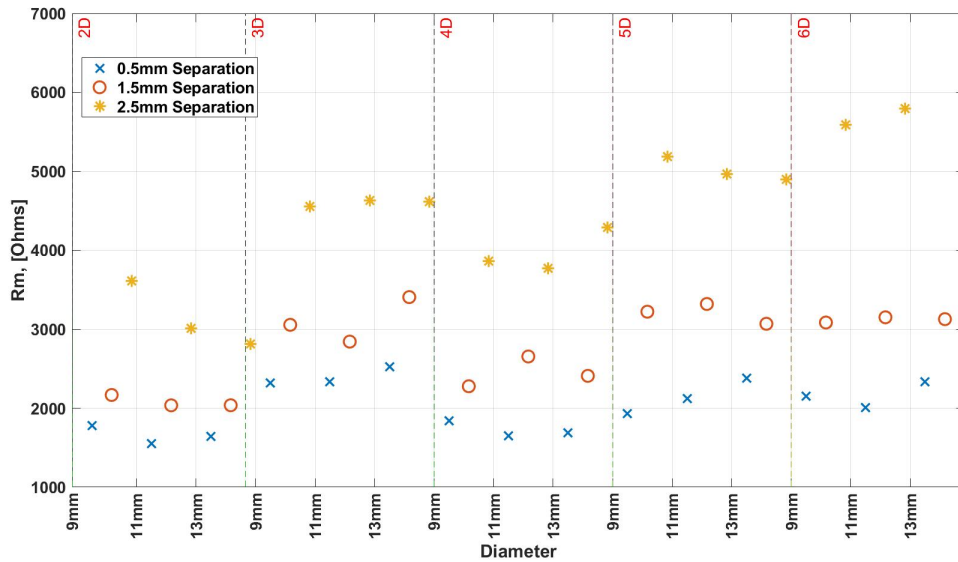
Figure 3.8. Motional resistance of unloaded bare LFE devices for the Slow Shear mode.

In Figure 3.9 the measured bandwidth of each bare LFE device has the trend of decreasing as electrode separation increases, further enforcing that narrower electrode separation improves the overall performance of the sensor. The highest

average measured bandwidth,75Hz ±5Hz, is also found to be for the 2 Diopter
samples.
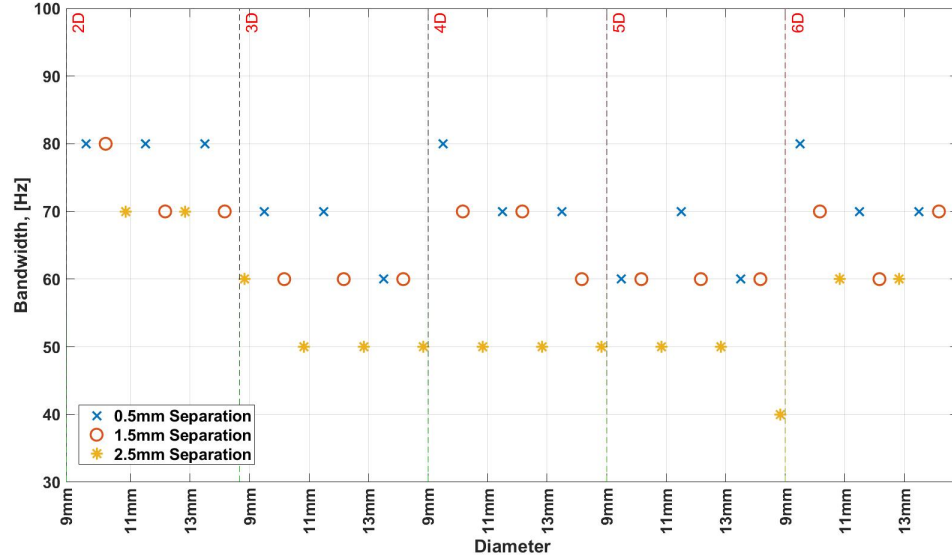
Figure 3.9. Separation between f_s and f_p of unloaded bare LFE devices for the Slow
Shear mode.

The bare LFE devices also show that the derived C_r, Figure 3.10, has a direct
relationship with the electrode separation, increasing as the separation increases.
For both the C_r and bandwidth, the diameter of the electrodes appears to have
minimal impact on these parameters.

3.3.2.2   Fast Shear Mode

Comparing the results from the Fast Shear mode and the Slow Shear mode, R_m
shows the same trend of decreasing as electrode separation decreases and as surface
curvature is decreased. Overall the R_m for the Fast shear mode, Figure 3.11,
appears to yield smaller values, with a minimum of 1334Ω compared to a minimum
of 1548Ω for the Slow Shear mode.
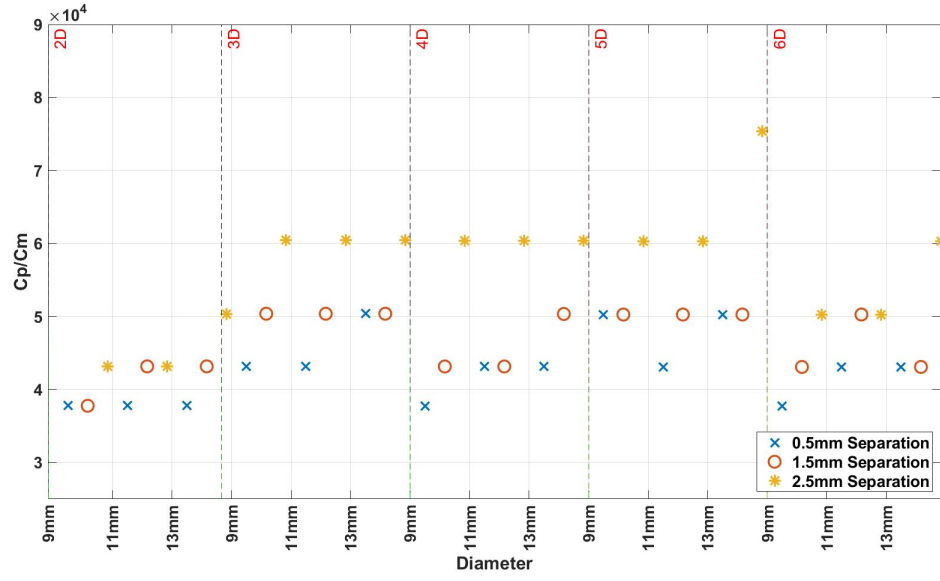
Figure 3.10. Capacitance ratio of unloaded bare LFE devices for the Slow Shear mode.
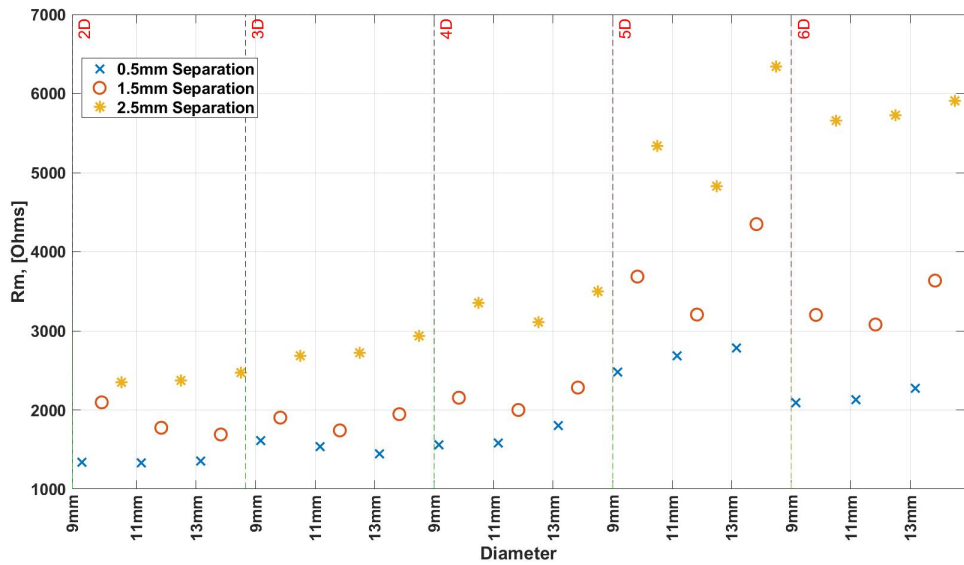
Figure 3.11. Motional resistance of unloaded bare LFE devices for the Fast Shear mode.

The bandwidth for the Fast Shear mode, Figure 3.12, and the C_r, Figure 3.13, show similar results to those found for the Show Shear mode, Figure 3.9 and Figure 3.10 respectively.

27
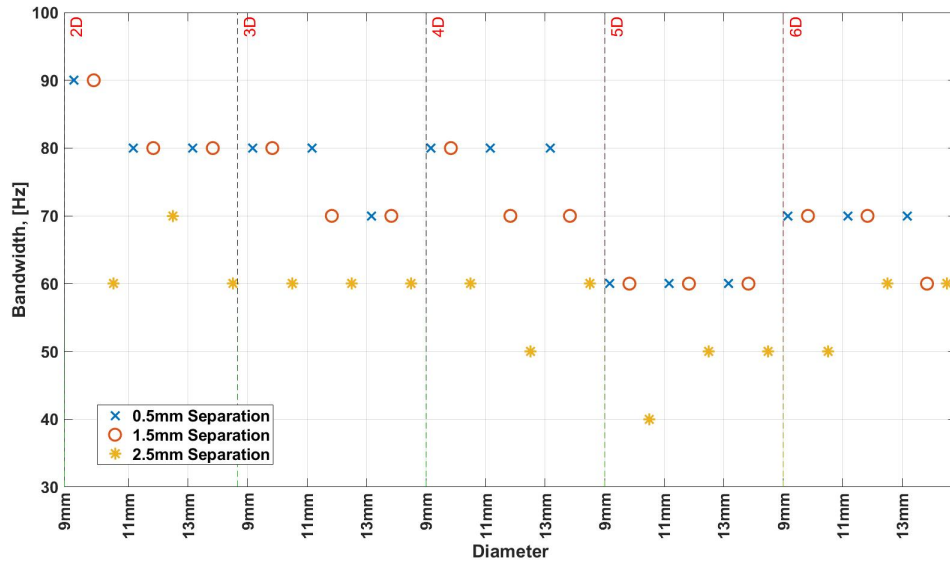
Figure 3.12. Separation between f_s and f_p of unloaded bare LFE devices for the Fast Shear mode.
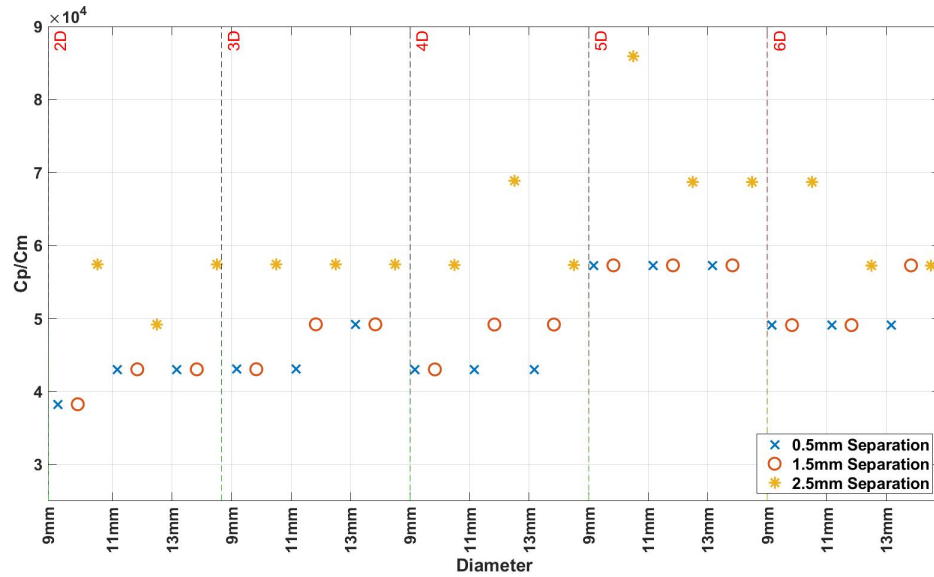
Figure 3.13. Capacitance ratio of unloaded bare LFE devices for the Fast Shear mode.

From comparing all of the data collected on each of the samples, the optimum configuration for the LFE appears to be 2 Diopter samples with a 0.5mm electrode separation. Furthermore, the response of the LFE is improved when the electrode

configuration is placed on the sensor holder instead of being directly deposited onto the surface. No distinct trends on the parameters extracted were found relating to the electrode diameter. However, looking at only the 2 Diopter LFE devices with deposited electrodes and a separation of 0.5mm, the 11mm diameter had the lowest R_m at 2256Ω and a low Q factor of 12.22k. The Fast Shear mode did have a smaller R_m. However, the current design for the electrical interface requires the electrodes to be deposited on the LFE and all fabricated LFE devices were for the Slow Shear mode. Therefore the LFE configuration used for mass loading for testing the electrical interfaces used the Slow Shear mode, had a surface curvature of 2 Diopter, 0.5mm electrode separation, and diameter of 11mm.

CHAPTER 4
DESIGN & TESTING OF ELECTRICAL INTERFACE SYSTEMS

An electrical interface needed to be developed for the LFE in order to use the LFE sensor. Previous attempts to develop an electrical interface for the LFE using oscillator based interface have proven unsuccessful[24, 25, 26]. With this in mind, alternative oscillator based interfaces were investigated for potential use with the LFE sensor: the Clapp oscillator, the Miller oscillator, and the Pierce oscillator configurations. Furthermore, the Balanced Bridge oscillator was investigated and developed to reduce the impact of the parallel capacitance, C_p, seen by the LFE sensor. The final interface investigated was a phase-mass based system. This system, the Phase-Shift Monitoring system, excites the sensor using an external source and then monitors the phase difference between the sensor and a constant reference branch.

To determine the potential for each system, they were designed and simulated using a 6MHz TFE device BVD parameters. This was then used as a benchmark for designs of each system for the LFE sensor. The BVD parameters for the TFE and LFE sensors are shown in Table 4.1. These parameters were used in the design process of each system to set the values of the passive components.

Table 4.1. BVD parameters for LFE & TFE sensors.

Component	LFE	TFE
C_p	1.26pF	9.94pF
L_m	23.6746H	26.6mH
C_m	29.47aF	26.5fF
R_m	2039Ω	54Ω

The Balanced Bridge and Phase-Shift Monitoring systems were fabricated and tested with a 6MHz reference crystal, a TFE device and a LFE device. Both circuits

were designed to operate with ±5V supplies. All simulations were done with Micro-Cap 11.

A Rigol DP832 programmable DC power supply was used as the power supply for the experiments. A Siglent SDG 1032X function/arbitrary waveform generator was used to generate reference signals. A Rigol DS1054Z oscilloscope and a Digilent Analog Discovery unit were used for measuring the systems response.

4.1   Clapp, Miller and Pierce Oscillator

The three conventional oscillator configurations that were selected where the Miller, Pierce and Clapp oscillators as shown in Figure 4.1.
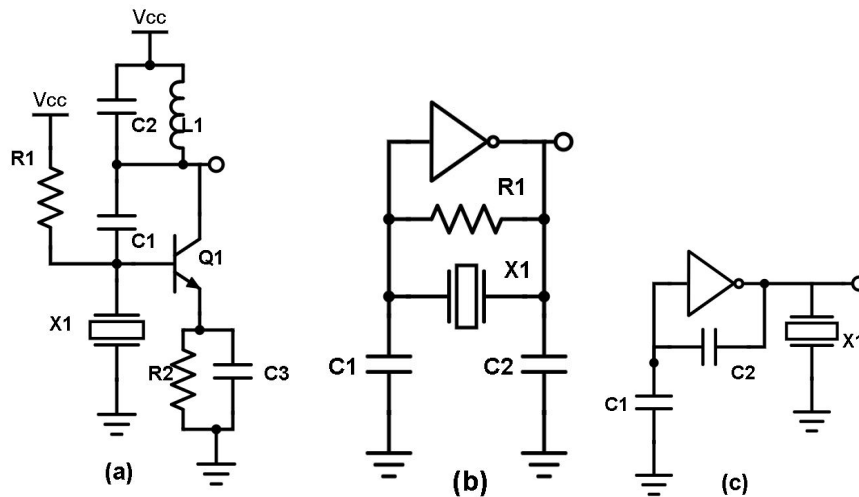
Figure 4.1. Miller oscillator (a) Pierce oscillator (b) and Clapp oscillator (c).

The Miller oscillator configuration shown in Figure 4.1 was based on a design proposed for high load impedance crystals[8]. This configuration also has one of the electrodes tied to ground, which helps reduce C_p seen by the sensor. The feedback capacitor, C1 in Figure 4.1(a), was set to 4.7pF and 1pF for the TFE and LFE design respectively. The value of this capacitor were tested over a range off 1s of pF to 10s of nF before selecting final component values for both the TFE and LFE case.

This was also done for the C1 and C2 in Figure 4.1.(b, c) for both the Pierce and Clapp oscillator simulations. The simulated Miller oscillator is shown in Figure 4.2.
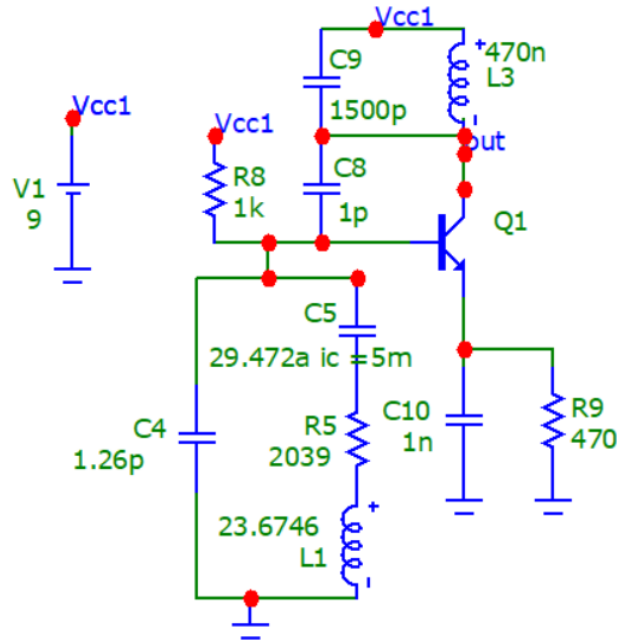
Figure 4.2. Simulated Miller oscillator with LFE BVD parameters.

The Miller oscillator uses an common emitter to invert the input signal, achieving 180° of phase shift. The LC tank formed by C2 and L1 in Figure4.1(a) is tuned to be inductive at the series resonance of the sensor and provides a 90° phase lead. C1 and the sensor provide another 90° phase shift at the operating frequency, netting a total phase loop of 360°. The Miller oscillator was simulated using a 9V supply and a 2N3904 transistor. Figure 4.3 shows the simulated response at the output (red) and as the base of the BJT (blue) with both the LFE and TFE BVD parameters.

Analyzing the simulated responses of the Miller oscillator shown in Figure 4.3, the TFE was able to achieve a stable oscillation at the expected 6MHz. The LFE was not able to achieve a stable oscillation frequency.

The Pierce oscillator as seen in Figure 4.1(b) is a commonly used electrical interface for QCM devices, for its frequency stability, as well as its simple and
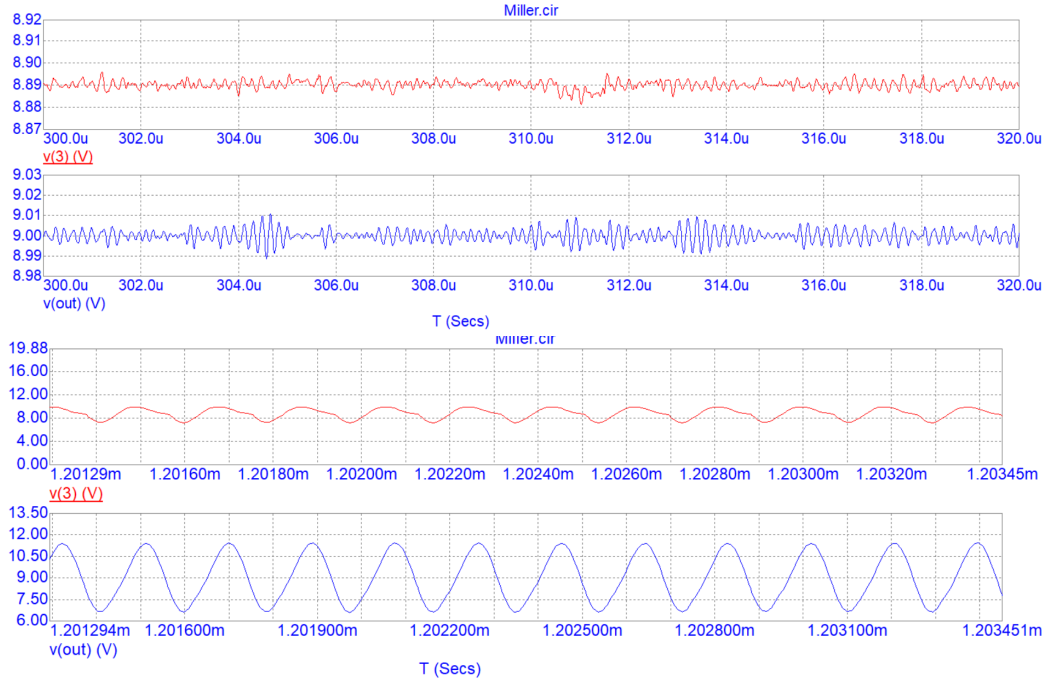
Figure 4.3. Simulated Miller oscillator with LFE (Top) and TFE (bottom) BVD.
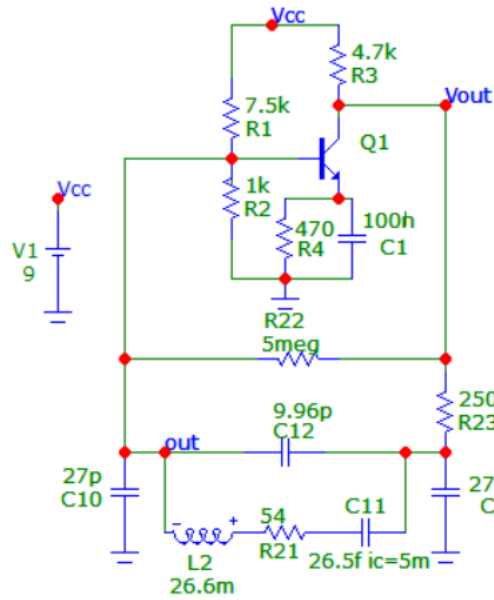
Figure 4.4. Simulated Pierce oscillator with LFE (bottom) and TFE (top) BVD.

compact design. The Pierce oscillator places the sensor in the feedback loop of a high gain inverting amplifier to achieve it's zero-phase shift oscillation requirement. The feedback resistor, R1 of the Pierce oscillator in Figure 4.1, causes the amplifier

to have a high gain and inverting output [9]. The capacitors C1 and C2 along with the sensor form a π-network, having a phase shift of 180°.
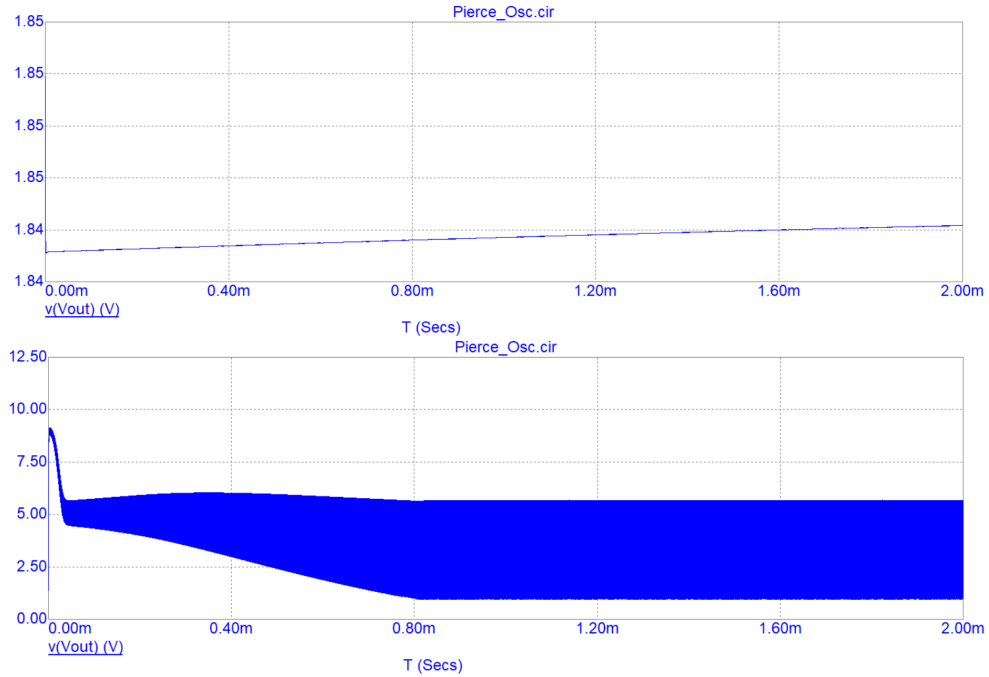
Figure 4.5. Simulated Pierce oscillator with LFE (Top) and TFE (bottom) BVD.

The Pierce oscillator was simulated using a 9V supply and a 2N3904 transistor. The simulated Pierce oscillator circuit is shown in Figure 4.4. To start the oscillation, the motional capacitance is given an initial current, then the simulation runs long enough for a stable oscillation to occur, as seen in Figure 4.5. For the TFE design, the pi network capacitors, C1 and C2 in Figure 4.1 are set to 27pF each, while for the LFE both were set to 2.4pF. This simulation shows that while the TFE sensor is able to achieve a stable oscillation after approximately 1ms, the LFE sensor is not able to achieve any level of oscillation.

The Clapp oscillator, Figure 4.1(c), configuration is a variation of the Colpitt's oscillator configurations that uses a common base amplifier instead of an common emitter, and has the benefit of grounding one of the electrodes on the sensor, reducing additional parallel capacitance seen by the sensor[10]. The total loop gain

34
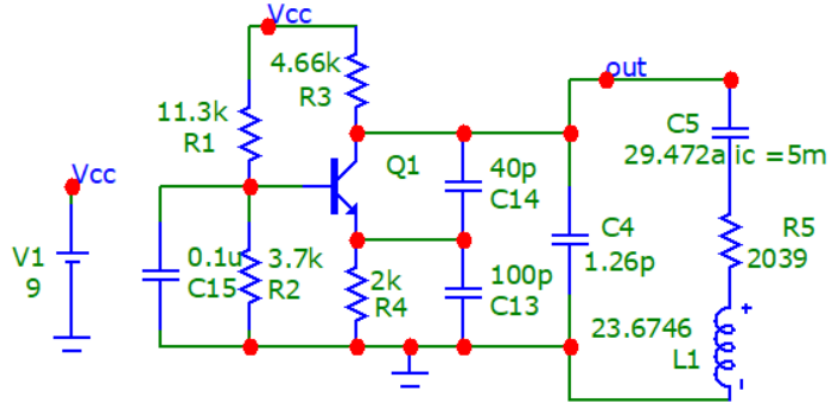
Figure 4.6. Simulated Clapp oscillator with LFE BVD parameters.

of this circuit is set by transconductance of the transistor, g_m, C1 and C2 as seen in Figure 4.1.

$$\frac{g_m}{(2\pi fs)^2 R_m C_1 C_2} < 1 \tag{4.1}$$

For the TFE design, C1 and C2 (Figure 4.1.c) were set to 40pF and 100pF respectively. For the LFE design, C1 and C2 were set tot 6pF and 18pF. The Clapp oscillator was simulated using a 9V supply and a 2N904, as shown in Figure 4.6.

The simulated results of the Clapp oscillator, shown in Figure 4.7, again demonstrate that the TFE sensor is able to achieve a stable oscillation, while the current configuration of the LFE sensor is not able to produce a stable output. This is due to the high motional resistance and the significantly smaller peak-to-peak response of the LFE.

4.2 Balanced Bridge Oscillator

Section 4.1 and the previous attempts at developing an oscillator based interface for the LFE sensor[24, 25, 26] were unsuccessful due to the high motional resistance and high Q factor, it was clear that the LFE would require more precision in design and component selection achieve a stable oscillation. Additionally, it was realized
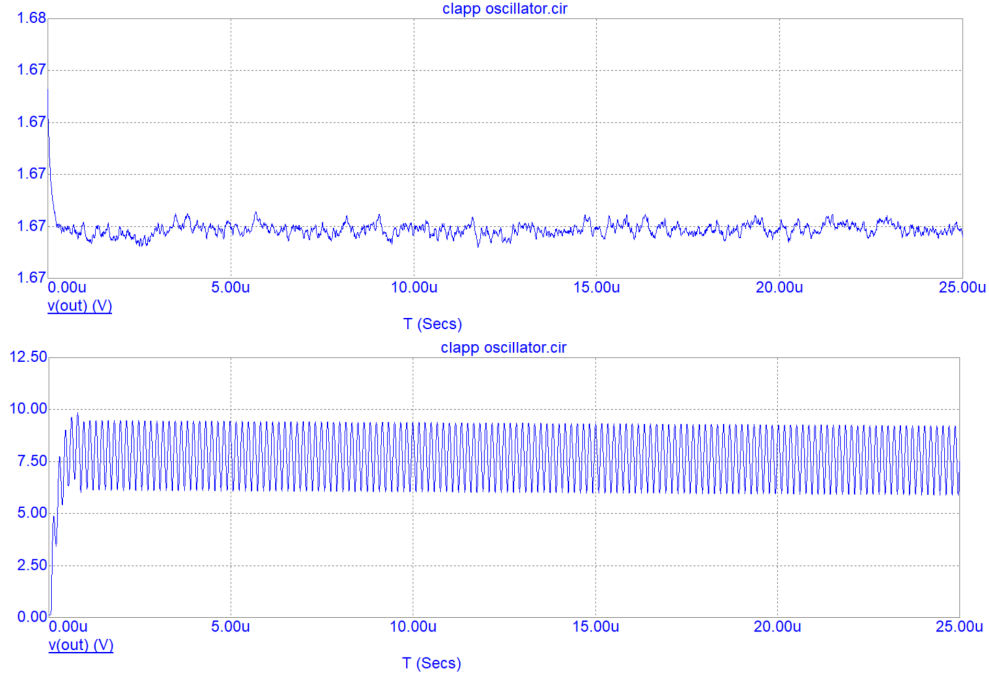
Figure 4.7. Simulated Clapp oscillator with LFE (Top) and TFE (bottom) BVD.

that reducing the parallel capacitance seen by the LFE to just the parallel plate capacitance would increase the bandwidth and therefore lower Q. The Balanced Bridge oscillator, Figure 2.6, was initially proposed to compensate for the parallel capacitance a QCM would see when connected with a coaxial cable [11]. This system uses a tuning capacitor, C_v, in the opposite branch from the LFE to reduce the parallel capacitance seen by the sensor. One of the branches was simulated with the LFE and then TFE BVD equivalent circuits as shown in Figure 4.8.

The simulation was done using a excitation signal, V1, to represent the feedback of the system. In the RLC branch, the resistor, R7, was set as close to R_m as possible using E24 standard resistor values. The LC tank was tuned to series resonant frequency of the sensor, approximately 6MHz. The AC operation was simulated using both the LFE and TFE BVD equivalent circuits as well with C_v, as shown in Figure 4.9.

As shown in Figure 4.9, the TFE and tuning capacitor showed a clear response at the resonance, however, the LFE did not. Where the circuit was simulated with a

36
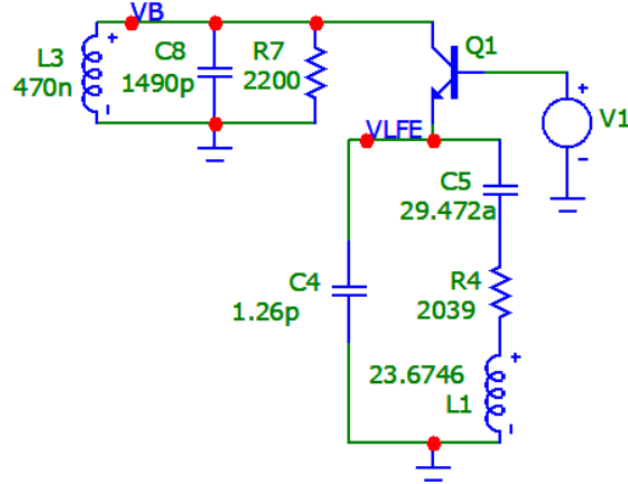
Figure 4.8. Simulated Balanced Bridge sensor branch with LFE BVD parameters.

2N3904 transistor, the circuit may be improved through the use of a Operational Transconductance Amplifier (OTA)[27]. With this in mind, a PCB, Figure 4.10, for the system was developed.

The Balanced Bridge oscillator was designed using OPA860 OTAs, a LM311 comparator, SA602A mixer, and an AD835 AGC stage. The mixer for the circuit was selected to be the SA602A. R_c was selected to satisfy (2.16), where AD is approximately unity [29] and the R_m range was estimated to be between 1.5kΩ and 10kΩ. Rc was selected to be 1kΩ for initial testing with the LFE samples on hand. L_c was set to 470nH and C_c was set to 1.5nF. C_v was replaced with a trimmer cap to allow for tuning. The system was first tested with the sensor left as an open and a 6MHz clock crystal ATS060B-E in place of the sensor, as shown in Figure 4.11.

When the sensor is left open, the system outputs a 300mVpp signal with a frequency of 5.98MHz. With the clock crystal, the output signal increased to a nearly 2Vpp signal with a 6MHz frequency. However, when the LFE was connected to the Balanced Bridge system, the output signal was unstable and did not maintain a consistent frequency. Several different values were tried for the tuning capacitor, but the output remain unchanged.
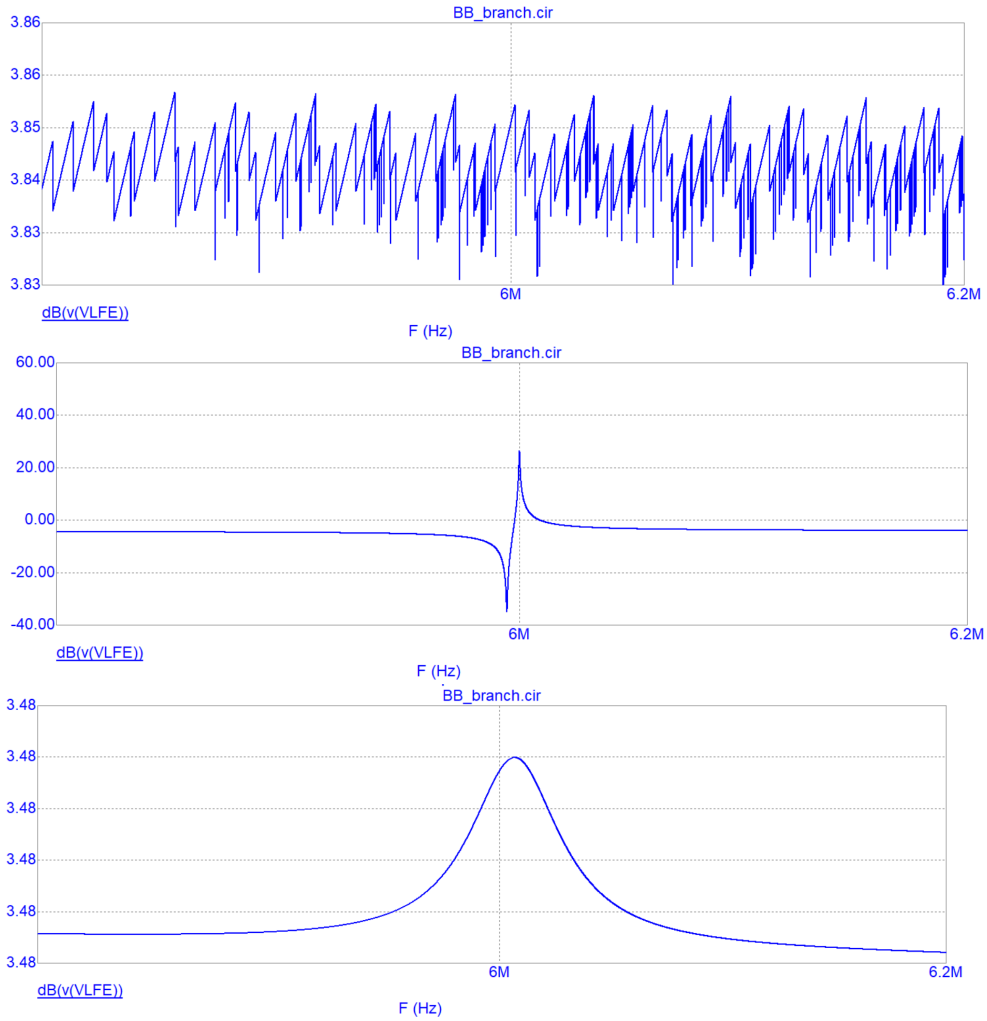
Figure 4.9. Simulated Balanced Bridge sensor branch oscillator with LFE (Top), TFE (middle) BVD, and reference capacitor (bottom).

4.3   Phase-Shift Monitoring System

Where attempts to achieve a stable oscillation with the LFE sensor have proven unsuccessful, a different method for tracking the sensor's response was investigated. The Phase-Mass method, as shown in (2.17), relates the change in mass on the sensing surface of the sensor to the change in the frequency shift at a given excitation frequency[12]. The Phase-Shift Monitoring system, shown in Figure 2.8, was developed to use this method and was proven the be up to three times more sensitive to mass changes than frequency tracking systems[27].

38
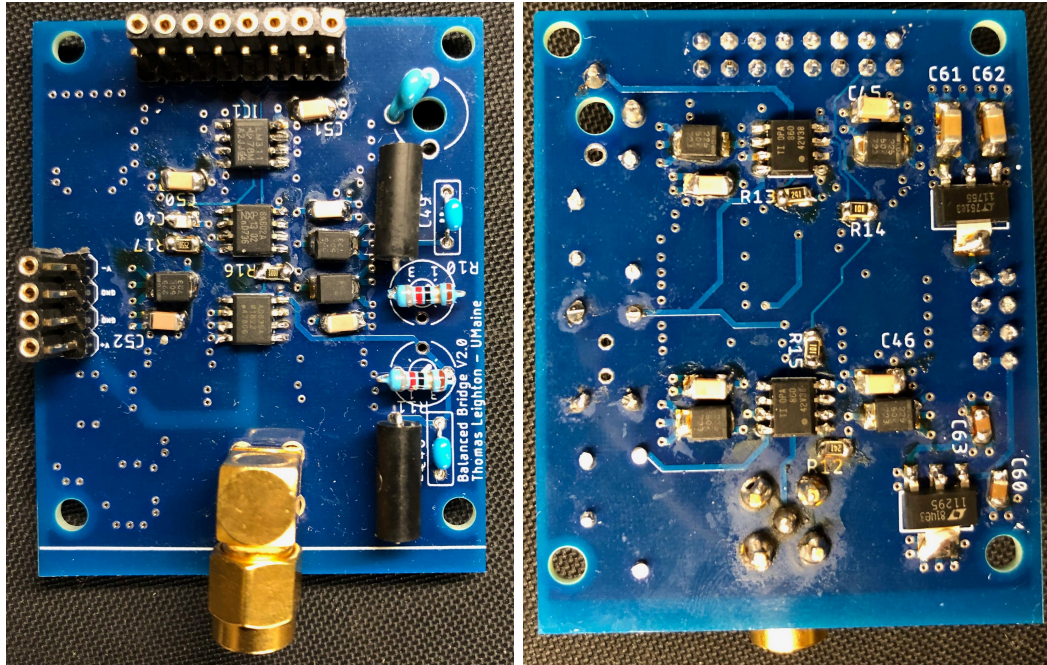
Figure 4.10. Balanced Bridge test circuit.

The Phase-Shift Monitoring system uses an external reference signal to excite the sensor at that fixed frequency, ideally the resonant frequency. The AD8302 from Analog devices measures the gain and phase-shift difference between the two branches. The passive filters at the input of the system provide an initial 90° offset between the sensing branch and the reference branch.

To initially test the system's response, the sensor branch of the system was simulated, Figure 4.12. The AC gain and phase shift of the sensing branch was simulated with both the LFE and TFE BVD equivalent parameters, as shown in Figure 4.13.

Comparing the simulated results in Figure 4.13, the TFE shows a clear response at its resonant frequency, while the simulated LFE output shows only a Linear slope for both the AC gain and phase-shift response. The reference components, R_c and C_c in Figure 2.8 were set to 2200Ω and $1.5pF$ respectively.

The RC filters at the input of the circuit were set to have a cutoff frequency at 6MHz, to ensure a 90° phase-shift difference between the two branches at the

39
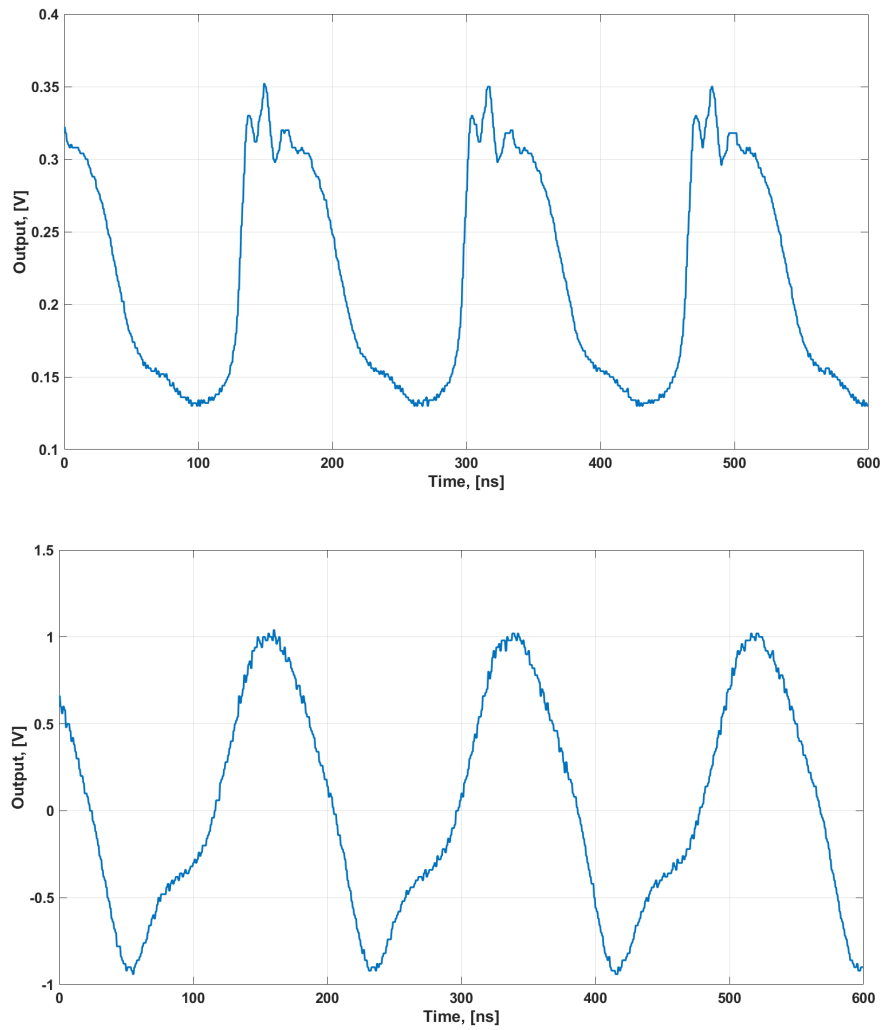
Figure 4.11. Measured Balance Bridge response with sensor open (top) and 6MHz clock crystal (Bottom).

resonant frequency. Further tuning could be done to these filters for a more precise cut off, but where they are only first order filters and the phase-shift output can easily be tuned using the reference voltage V_{ref1} at the gain stage. The 6MHz cutoff is sufficient to make the circuit preform as intended. R_t was set to 2200Ω, a value near the motional resistance derived for the LFE of 2039Ω. The system was built on a 4 layer PCB for testing, as shown in Figure 4.14.

The test circuit for the Phase-Shift Monitoring system was designed to use ±5V supplies. The system was biased with an 8Vpp sinusoidal signal at 6025247Hz, the
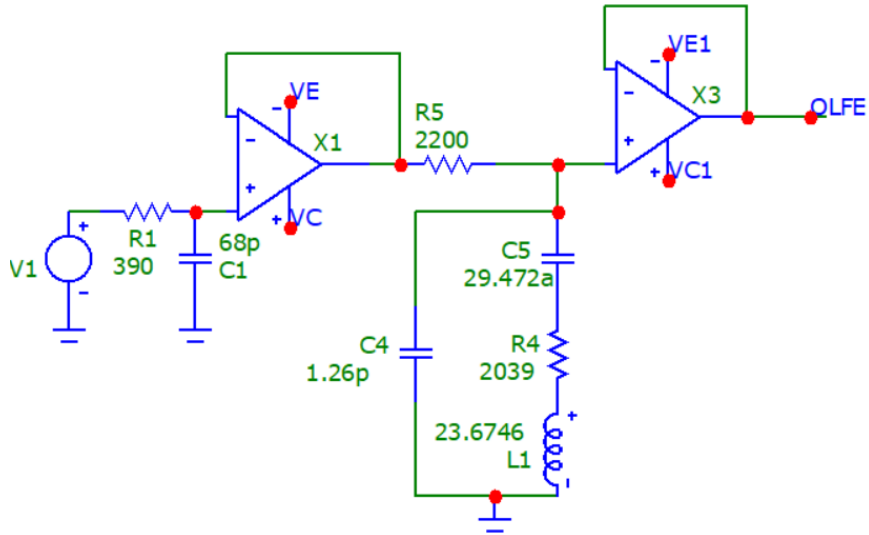
Figure 4.12. Simulated Phase-Shift Monitoring system sensor branch with LFE BVD parameters.
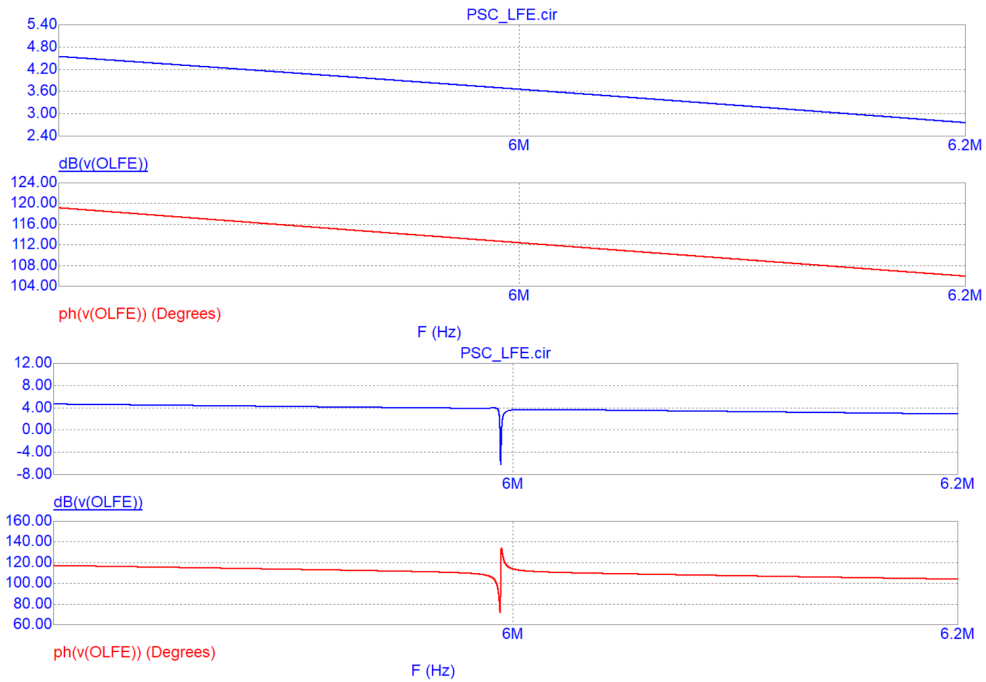
Figure 4.13. Simulated Phase Shift Characterization sensor branch with LFE (Top) and TFE (bottom) BVD.

measured series resonance frequency of the selected LFE sample. To create more consistent placement of the sensor on the PCB and help prevent movement,
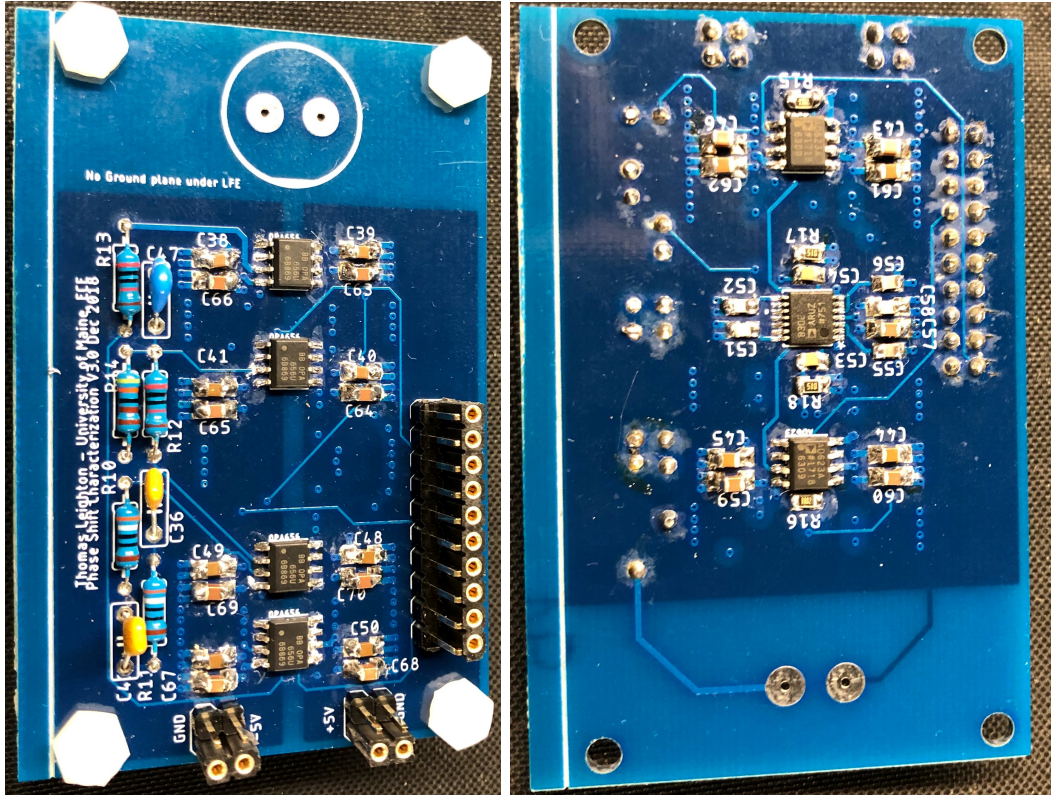
Figure 4.14. Developed Phase Shift Monitoring system test circuit.

electrical tape was used to construct a sample holder on the PCB. The

measurement set up is shown in Figure 4.15
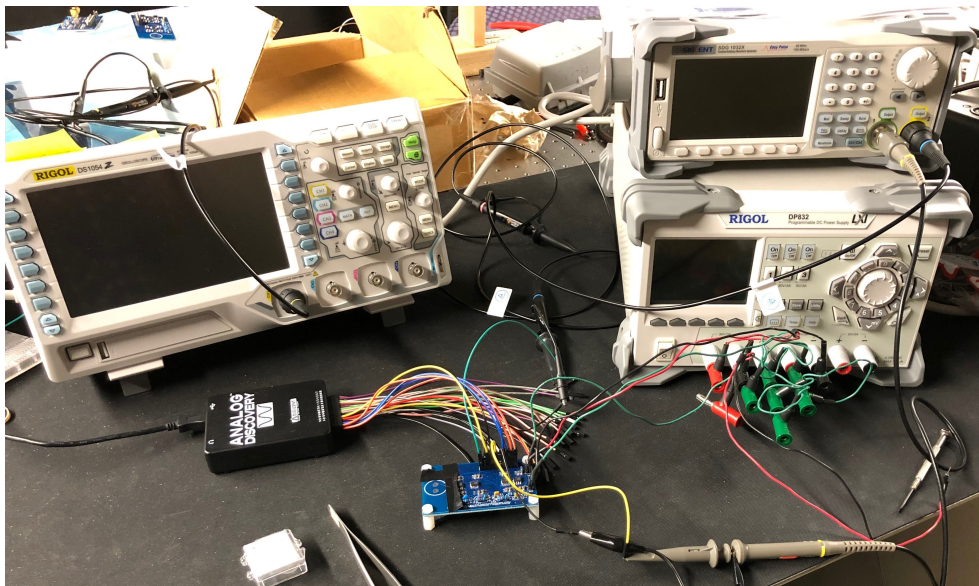
Figure 4.15. Measurement setup for testing the Phase-Shift Monitoring system.

First the system was tested with the unloaded LFE on the PCB and then with the sensor position left open. The system detected approximately a 28° difference in the absence of the sensor. Before testing the system further the outputs V_ψ and V_A were set to zero by adjusting the reference voltages, V_{ref1} and V_{ref2} at the input of the amplification stage. The outputs were measured as averages over ten second spans. Once the system had warmed up and the unloaded LFE was on the PCB, it was realized that the output average V_ψ would drift by ± 0.6mV over the period of a few minutes.

The signals from the reference and LFE branch, u_1 and u_2 respectively, were also measured to determine phase shift between the branches. Figure 4.16 shows the measure response from u_1 and u_2 with the LFE with no mass loading.
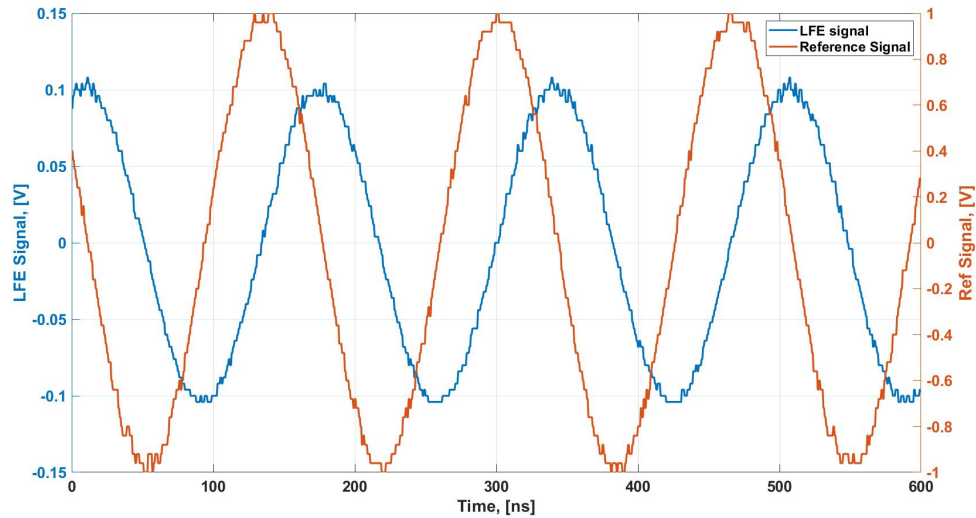
Figure 4.16.   Measured transient signals from reference and sensor branches with the LFE unloaded.

The recorded difference in phase-shift between the two branches was -92° when the LFE is not loaded. This matched the 924mV (10m/^{o} before amplification) offset required to tune the output $U\psi$ to 0V. When the LFE was loaded, the phase difference was -86° and the measured $U\psi$ was approximately 645mV, or a change in the phase of 6.45^o between the loaded and unloaded instances. The measured

43

phase-shift difference would vary by $\pm 2^o$ when using the Rigol DS1054Z oscilloscope. Considering this tolerance set by the equipment used, this shows that the AD8302 is able to detect the difference in phase-shift between the two branches.

Since the system cannot be placed in a deposition chamber in its current setup, an alternative method for testing the systems output to small mass changes detected by the LFE sensor. Initially the system was tested using $0.2\mu L$-$2\mu L$ pipette by Fisherbrand to test liquid loading. This method proved to have too many flaws to continue. The minimum mass that could be deposited with this method was approximately $200\mu g$, and due to the surface curvature of the sensor the liquid would wrap around the edges of the sensor. Furthermore, liquids like isopropanol would evaporate quickly preventing accurate tests. Additionally, this would result in viscous loading as well as mass loading. Where the goal of these initial measurements were the test the system with a purely mass loading source, an alternate testing method had to be used.

The next method attempted was by using kimwipes by Kimtech Science as a mass source. For this approach, a single tissue was weighed and found to be 0.4846g. The dimensions of a single tissue are $8\frac{3}{8}$" by $4\frac{3}{8}$". Therefor a $\frac{1}{16}$" square of the tissue should weigh approximately $52\mu g$. This approach was used since the available scale was accurate only down to the 100s of microgram range. Due to the inconsistency of the thickness of the tissue, contaminants, and tolerance set by human error in cutting the piece, this mass will only be used as a general range. The first test was for consistency of the system and sensor. This was done by recording the systems outputs bare, then with then the mass loaded close to the center of the sensor. During this measurement it was noted that placement of the mass on the LFE would change the response, where the further the mass was from the center, the lower the change in the systems response would be. The recorded change in V_ψ for each measurement is shown in Figure 4.17.
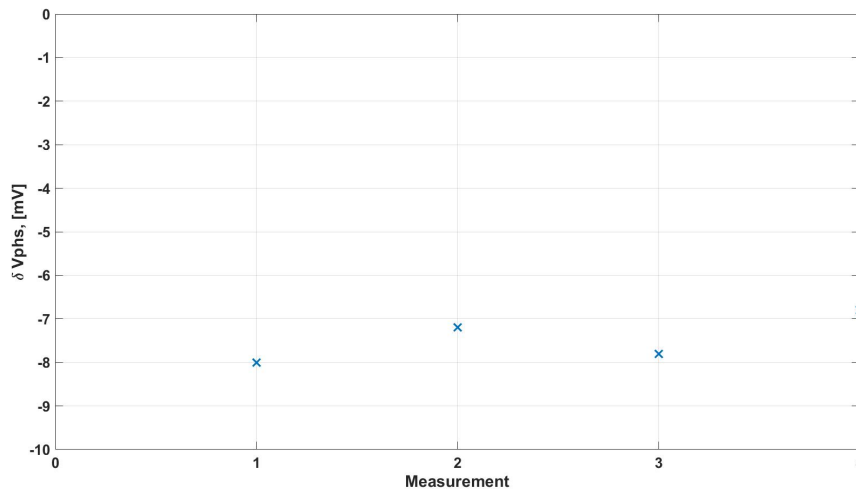
Figure 4.17. Change in out V_ψ for repeated measurements with same mass.

The average recorded change in V_ψ was -7.45mV, or -0.00745^o phase-shift. The separation between the minimum and maximum values was 1.2mV or an error of $\pm 8.05\%$ for this measurement. For this measurement there were several potential sources of error. The mass did not sit flush to the surface every time, creating an uneven distribution in the mass. The mass was also subject to human error in the placement mass on the sensor. Since the measurements were not done in a vacuum, contaminants could be on the surface of the sensor or cling to the mass. Additionally, any noise in the system itself would contribute to error in the output.

To show the relationship between phase-shift and change in mass, another set of measurements were made. For this set the three different squares of tissue were used as a mass loading source, and loaded one at a time on the LFE. Each was first tested individually and the average change in V_ψ was found for each. These averages were then used to represent the relative mass of each sample added. The final measured results are shown in Figure 4.18.

During these measurements it was found that stacking the mass samples on top of each other would result in a significantly diminished response compared to when the mass was placed directly onto the sensor. For that reason, the masses were
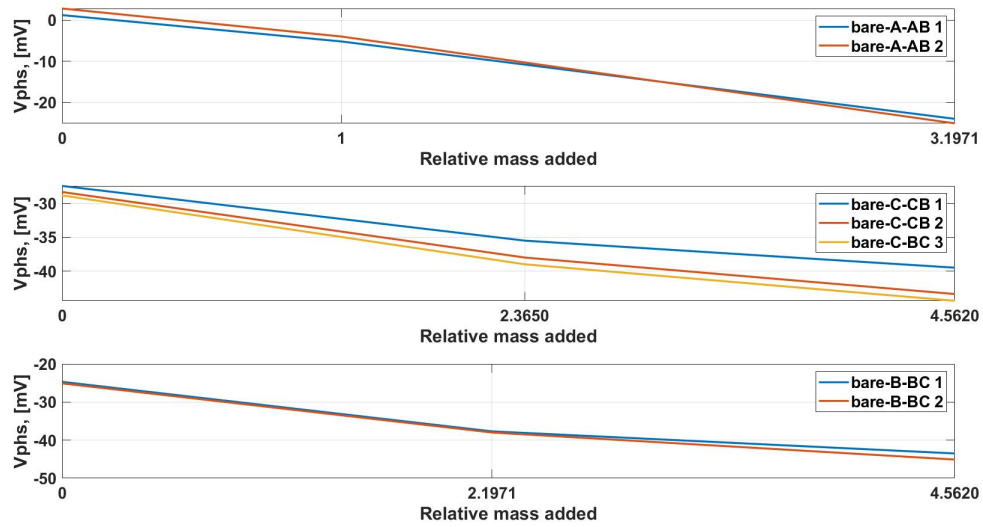
Figure 4.18. Measured V_ψ versus relative mass added.

placed directly next to each other close to the center of the sensor. This also made it difficult to add more sources of mass as each additional mass source was further from the center, and therefore had an increasingly diminished response. To reduce the many sources of error found in these measurement the Phase-Shift monitoring with the LFE sensor should be tested in a deposition chamber. These results appear to be similar to the results found for when the same system was tested using a TFE sensor and liquid loading, as shown in Figure 4.19[27].
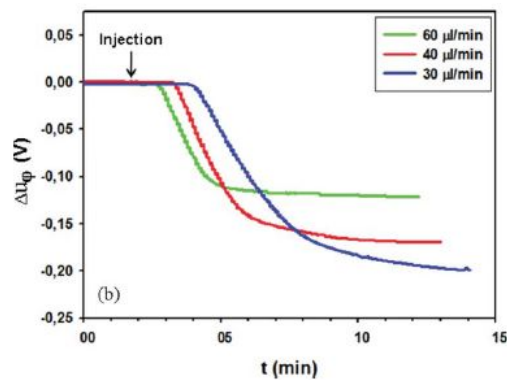
Figure 4.19. Measured V_ψ as a liquid load is deposited onto the surface of a TFE sensor.

Antonio Arnau described the relationship between phase and mass shown in Figure 4.19 as exponentially decaying. However, the initial injection in Figure 4.19 appears to have a close to linear relationship until a saturation point is reached. This linear slope is similar to the relationship derived for the phase-mass relationship for the Phase-Shift Monitoring system[12].

$$\Delta\varphi = -\frac{\Delta m_c}{m_q + m_L}\frac{R_t}{R_t + R_m} \qquad (4.2)$$

Where $\Delta\varphi$ is the phase difference between the sensor branch and the reference branch, Δm_c is the change in the coating mass, m_q is the effective surface mass of the quartz resonator, and m_L is the equivalent surface mass density associated with the oscillatory movement of the surface of the sensor in contact with a fluid medium. Further testing on the phase-mass relationship with the LFE sensor is required to verify the relationship described by (4.2).

CHAPTER 5
SUMMARY, CONCLUSIONS, AND FUTURE WORK

5.1 Summary

There are two types of electrode configurations for the QCM, Thickness Field Excitation (TFE), and Lateral Field Excitation (LFE). The LFE configuration has the sensing surface bare, allowing LFE devices to detect not only mechanical changes like TFE devices, but also changes in electrical properties. Until now there have been no electrical interfaces developed for the LFE configuration.

This thesis has presented background on Quartz Crystal Microbalance (QCM) resonators, describing both the TFE and LFE configurations. LFE and TFE sensors were modeled using the Butterworth-Van Dyke (BVD) lumped circuit equivalent model, and the impacts the each parameter has on the impedance response of the sensor were presented. Five electrical interface systems, including Clapp oscillator, Pierce oscillator, Miller oscillator, Balanced Bridge oscillator, and Phase-Shift Monitoring system were investigated, designed and tested.

The impact variations in the LFE sensor's surface curvature, electrode diameter, and electrode separation had on the sensor's admittance response was investigated. The BVD equivalent circuit was used to model the measured admittance response of the 45 fabricated sensors. This information was used to identify which configuration for LFE devices preformed the best in terms of motional resistance, separation between resonance frequency and peak-to-peak impedance response. Additionally, the BVD model was used to design the electrical interfaces.

The Clapp, Miller, and Pierce oscillator systems were investigated and tested with both TFE and LFE devices to determine why conventional oscillator-based systems have failed in previous studies. The Balanced Bridge oscillator system was

investigated, developed and tested for potential implementation as the electrical interface with LFE devices. The Phase-Shift Monitoring system was constructed and tested with LFE devices. This Phase-Shift Monitoring system's response was used to test the LFE sensor's phase-shift response to mass loading.

5.2 Conclusions

The purpose of this thesis was to develop an electrical interface for the LFE sensor. Additionally, this thesis identified an optimum configuration from 45 fabricated LFE devices. From the measured admittance response of each LFE configuration, the BVD parameters were derived for each of the fabricated LFE devices. Using the derived BVD parameters, the LFE configuration was determined to have the best response in terms of smallest motional resistance and highest separation between resonance frequencies. The identified configuration has a surface curvature of 2Diopter, an electrode separation of 0.5mm and a electrode diameter of 11mm. This LFE configuration had the lowest R_m (2036Ω) among the tested LFE devices and a bandwidth of approximately 110Hz.

The Clapp, Pierce and Miller oscillator systems were all found to be unable to achieve a stable oscillation with current configurations of LFE devices operating in air or vacuum media. This was due to the sensor's high motional resistance, Rm, and high capacitance ratio, Cr, compared to equivalent Thickness Field Excited (TFE) sensors. This resulted in the LFE having a significantly smaller peak to peak impedance response with a much narrower bandwidth than the TFE sensor. The Balanced Bridge oscillator also proved unable to achieve a stable oscillation with the LFE sensor.

The Phase-mass method was investigated as an alternative to the frequency tracking method. Using this method, the Phase-Shift Monitoring system was developed. This system was successful at consistently detecting mass changes in the

μg range outside of a vacuum chamber. This system outputs two DC signals corresponding to the phase-shift difference (100mV/^{o}) and the magnitude difference (300mV/dB) between the sensing branch and the reference branch.

The Phase-Shift Monitoring system has proven to be compatible with the LFE for mass sensing applications in air and vacuum media. The phase-mass method has been proven to work for the LFE sensor where oscillator based systems have been unsuccessful for current configurations of the LFE sensor. When the LFE was loaded with $52\mu g$ in air, the Phase-Shift Monitoring system output 7.45mV (0.00745^o) with a tolerance of ± 0.6mV. This system proven to be capable of using the LFE sensor to detect any level of mass change on the sensing surface.

5.3 Future Work

While the Phase-Shift Monitoring system has been shown to operate with the LFE sensor to monitor mass changes in the 10s of microgram range in air, there are several tasks to be completed on the system. First, the system needs to be integrated with a microcontroller to convert the system's output and calibrate the system. This can be done by using the analog ports on a microcontroller to read the DC outputs of the system and then convert them to the corresponding phase-shift change and magnitude change. Furthermore, the microcontroller could be used to automatically calibrate the reference voltages for new bare sensors. Also, the system could be improved to reduce sources of noise, such as from power supplies or signal generators.

The Phase-Shift Monitoring also needs additional testing to show the phase-mass relationship for a range of deposited masses. The ideal method for doing this would be to develop a holder for the LFE so that it can be placed in a deposition chamber separate from the interface. Then the deposition system would be used to deposit mass on the sensor at a known rate using a TFE as a rate

monitor, and record the detected change in the phase-shift. Once the phase-mass relationship of the LFE has been determined, the deposition system could also be used to characterize the phase-shift relationship to electrical properties, such as permittivity and conductivity, of the deposited material as well.

Further testing on the LFE sensor configuration should be done. The trend found for the fabricated LFE devices showed that reducing the electrode separation reduced the motional resistance, therefore, reducing the electrode separation further should be tested to see if this trend continues and potentially further improve the sensors response. Where plano-plano LFE sensors have been proven to an ineffective configuration [6], 1Diopter samples may prove to have improved performance with the current electrode configurations, since the trends shown by the derived BVD parameters revealed improved performance for sensors with lower surface curvatures. However, alternate electrode configurations and energy trapping structures for the LFE should be investigated to reduce R_m and increase the peak-to-peak response of the LFE.

REFERENCES

[1] Martin, S. J., Frye, G. C., & Wessendorf, K. O. (1994). *Sensing liquid properties with thickness-shear mode resonators*. Sensors & Actuators: A. Physical, 44(3), 209-218. doi:10.1016/0924-4247(94)00806-X.

[2] Arnau, A. (2008). *A review of interface electronic systems for AT-cut quartz crystal microbalance applications in liquids*. Sensors (Basel, Switzerland), 8(1), 370-411. doi:10.3390/s8010370

[3] Hu, Y., French, L. A., Radecsky, K., Pereira da Cunha, M., Millard, P., & Vetelino, J. F. (2004). *A lateral field excited liquid acoustic wave sensor*. IEEE Transactions on Ultrasonics, Ferroelectrics, and Frequency Control, 51(11), 1373-1380. doi:10.1109/TUFFC.2004.1367475

[4] Schmitt, R. F., Allen, J. W., Vetelino, J. F., Parks, J., & Zhang, C. (2001). Bulk acoustic wave modes in quartz for sensing measurand-induced mechanical and electrical property changes. Sensors & Actuators: B. Chemical, 76(1), 95-102. doi:10.1016/S0925-4005(01)00591-3

[5] Alassi, A., Benammar, M., & Brett, D. (2017). *Quartz crystal microbalance electronic interfacing systems: A review.* Sensors (Basel, Switzerland), 17(12), 2799. doi:10.3390/s17122799

[6] French, Lester A. (2011), *A Theoretical Model of a Lateral-Field Excited Sensor Element Under Liquid Loading.* Electronic Theses and Dissertations. 1636. https://digitalcommons.library.umaine.edu/etd/1636

[7] Jequil Hartz, unpublished works. 2019.

[8] Matthys, R. J. (1992). *Crystal Oscillator Circuits.* MALABAR, FL: KRIEGER PUBLISHING COMPANY.

[9] Titus, J. (2006). *It's crystal clear: Quartz still resonates with designers.* ECN-Electronic Component News, 50(11), 31.

[10] Gonzalez, G. (2007;2006;). *Foundations of oscillator circuit design.* Norwood: Artech House Inc.

[11] Benes, M. Schmid, M. Grűschl, P. Berlinger, H. Nowotny, and K. C. Harms, *Proceedings of the Joint Meeting of the European Frequency and Time Forum and the IEEE International Frequency Control Symposium,*Vol. 2, p. 1023âĂŞ1026 (1999).

[12] Arnau, A., Montagut, Y., Garcĺa, J. V., & Jimĺnez, Y. (2009). *A different point of view on the sensitivity of quartz crystal microbalance sensors.* Measurement Science and Technology, 20(12), 124004. doi:10.1088/0957-0233/20/12/124004

[13] Pinkham, W. A., & Vetelino, J. (2007). *A lateral field excited acoustic wave pesticide sensor.*

[14] McGann, Jason M. (2017). *Piezoelectric Platforms for Bulk Acoustic Wave Sensor Applications.* Electronic Theses and Dissertations. 2682. https://digitalcommons.library.umaine.edu/etd/2682

[15] Aepinus (1756). *"Memoire concernant quelques nouvelles experiences electriques remarquables" [Memoir concerning some remarkable new electrical experiments]* Histoire de l'Academie royale des sciences et des belles lettres (Berlin), vol. 12, pages 105-121.

[16] Curie, Jacques & Curie, Pierre. (1880). *"Developpement par compression de l'electricite polaire dans les cristaux hemiedres a faces inclinees" [Development, via compression, of electric polarization in hemihedral crystals with inclined faces].* Bulletin de la Societe Minerologique de France. 3: 90âĂŞ93.

[17] Gautschi, G. (2002). *Piezoelectric sensorics: Force, strain, pressure, acceleration and acoustic emission sensors, materials and amplifiers.* New York;Berlin;: Springer.

[18] Buttry, D. A., & Ward, M. D. (1992). *Measurement of interfacial processes at electrode surfaces with the electrochemical quartz crystal microbalance.* Chemical Reviews, 92(6), 1355-1379. doi:10.1021/cr00014a006

[19] Basics of a Quartz Crystal Microbalance. (n.d.). Retrieved from https://www.gamry.com/application-notes/physechem/basics-of-a-quartz-crystal-microbalance/

[20] Yihe Hu, L.A. French, K. Radecsky, M. Pereira da Cunha, P. Millard, J.F. Vetelino, *A lateral field excited liquid acoustic wave sensor* in IEEE Transactions on Ultrasonics, Ferroelectrics, and Frequency Control , vol. 51, no. 11, Nov. 2004, pp. 1373-1380 Available from: https://doi.org/10.1109/TUFFC.2004.1367475

[21] Sgambato, K. (2009). *Design and testing of a lateral field excited rate monitor for use in thin film deposition systems.* Electronic Theses and Dissertations. 937. https://digitalcommons.library.umaine.edu/etd/937

[22] *Quartz Crystal Oscillator and Quartz Crystals.* Basic Electronics Tutorials, 21 Feb. 2018, www.electronics-tutorials.ws/oscillator/crystal.html.

[23] Rosenbaum, Joel Frederick. (1988) *Bulk Acoustic Wave Theory and Devices.* Artech House

[24] Bennie McMinis III. (2017) *Oscillator Circuits for Lateral Field Excited Sensors.* Laboratory for Surface Science and Technology, University of Maine, 2017. PDF.

[25] Jordan Dykstra. *Oscillator Circuit for Portable Lateral Field Excited Acoustic Wave Sensor System NSF-REU Sensors!* UMaine 2014 (2014): 1-10. Pdf.

[26] Wallace, Samuel (2014). *Excitation of Bulk Acoustic Waves in Quartz Crystals.* Laboratory for Surface Science and Technology, University of Maine, 2014. PDF.

[27] March, C., Arnau, A., GarcÃŋa, J., Montoya, A., Montagut, Y., & JimÃľnez, Y. (2011). *Frequency-shift vs phase-shift characterization of in-liquid quartz crystal microbalance applications.* Review of Scientific Instruments, 82(6), 064702-064702-14. doi:10.1063/1.3598340

[28] Montagut, Y., GarcÃŋa, J. V., JimÃľnez, Y., March, C., Montoya, A., & Arnau, A. (2011). *Validation of a phase-mass characterization concept and interface for acoustic biosensors.* Sensors (Basel, Switzerland), 11(5), 4702-4720. doi:10.3390/s110504702

[29] Analog Devices, 250MHz, Voltage Output, 4−quadrant multiplier, AD835 Data Sheet (1994−2010)

[30] Jason M. McGann, Kristopher Sgambato, Donald F. McCann, and John F. Vetelino *Acoustic Mode Behavior in Lateral Field Excited Sensors.* 2009 IEEE International Ultrasonics Symposium Proceedings (209): 645-649. Pdf.

[31] Bryant, A., D. L. Lee, and J. F. Vetelino. *A Surface Acoustic Wave Gas Detector.* 1981 Ultrasonic Symposium (1981): 171- 74. Print.

[32] Vetelino, John, and Aravind Reghu. *Introduction to Sensors.* Boca Raton: CRC, 2011. Print.

[33] Benes, E., Groschl, M., Burger, W., & Schmid, M. (1995). *Sensors based on piezoelectric resonators.* Sensors and Actuators A: Physical, 48(1), 1-21. doi:10.1016/0924-4247(95)00846-2

[34] Wudy, F., Multerer, M., Stock, C., Schmeer, G., & Gores, H. J. (2008). *Rapid impedance scanning QCM for electrochemical applications based on miniaturized hardware and high-performance curve fitting.* Electrochimica Acta, 53(22), 6568-6574. doi:10.1016/j.electacta.2008.04.079

[35] Lu, F., Lee, H. P., & Lim, S. P. (2004). *Detecting solidâĂŞliquid interface properties with mechanical slip modelling for quartz crystal microbalance operating in liquid.* Journal of Physics D: Applied Physics, 37(6), 898-906. doi:10.1088/0022-3727/37/6/014

[36] Analog Devices, LF-2.7GHz, RF/IF Gain and Phase Detector, AD8302 Data Sheet (2002).

APPENDIX

APPENDIX A: MEASURED BVD PARAMETERS

Table A.1: BVD Parameters for Fabricated LFEs.

Diopter	Diameter [mm]	Separation [mm]	Rm[Ω]	Lm[H]	Cm[F]	Cp[F]
2	9	0.5	3249	7.241	9.67E-17	4.85E-12
2	9	1.5	2262	16.41	4.25E-17	1.83E-12
2	9	2.5	3159	7.354	9.46E-17	4.76E-12
2	11	0.5	2256	7.293	9.60E-17	4.81E-12
2	11	1.5	2236	61.76	1.13E-17	4.26E-13
2	11	2.5	3899	43.87	1.58E-17	7.97E-13
2	13	0.5	2521	24.03	2.92E-17	1.46E-12
2	13	1.5	2015	23.88	2.92E-17	1.10E-12
2	13	2.5	3822	128.4	5.42E-18	3.27E-13
3	9	0.5	6682	3.259	2.15E-16	3.08E-12
3	9	1.5	2300	29.1	2.39E-17	1.03E-12
3	9	2.5	3428	34.44	2.01E-17	1.01E-12
3	11	0.5	2507	10.82	6.46E-17	2.78E-12
3	11	1.5	4095	66.78	1.04E-17	6.29E-13
3	11	2.5	3704	9.223	7.52E-17	3.79E-12
3	13	0.5	2050	4.34	1.61E-16	6.93E-12
3	13	1.5	2785	8.92	7.80E-17	3.92E-12
3	13	2.5	3512	23.12	3.00E-17	1.51E-12
4	9	0.5	1825	9.01	7.76E-17	3.34E-12

Diopter	Diameter [mm]	Separation [mm]	Rm[Ω]	Lm[H]	Cm[F]	Cp[F]
4	9	1.5	3141	22.58	3.09E-17	1.86E-12
4	9	2.5	3988	35.86	1.94E-17	9.75E-13
4	11	0.5	2798	8.079	8.67E-17	5.21E-12
4	11	1.5	2849	8.321	8.36E-17	4.21E-12
4	11	2.5	4918	15.44	4.50E-17	2.72E-12
4	13	0.5	3210	10.07	6.95E-17	2.99E-12
4	13	1.5	3443	86.34	8.07E-18	4.05E-13
4	13	2.5	4217	66.03	1.05E-17	6.36E-13
5	9	0.5	2386	8.24	8.52E-17	4.26E-12
5	9	1.5	4678	13.57	5.15E-17	2.21E-12
5	9	2.5	4126	16.81	4.15E-17	2.08E-12
5	11	0.5	2010	6.283	1.12E-16	4.79E-12
5	11	1.5	6614	14.88	4.69E-17	2.36E-12
5	11	2.5	3609	19.15	3.64E-17	1.83E-12
5	13	0.5	3387	9.17	7.65E-17	3.83E-12
5	13	1.5	2720	7.716	9.05E-17	4.54E-12
5	13	2.5	3933	16.83	4.14E-17	2.08E-12
6	9	0.5	2653	95.48	7.36E-18	3.68E-13
6	9	1.5	3474	10.04	6.95E-17	3.49E-12
6	9	2.5	4831	42.33	1.65E-17	9.92E-13
6	11	0.5	1988	4.827	1.45E-16	6.24E-12
6	11	1.5	3360	7.843	8.90E-17	4.47E-12
6	11	2.5	4801	64.5	1.08E-17	6.51E-13

Diopter	Diameter [mm]	Separation [mm]	Rm[Ω]	Lm[H]	Cm[F]	Cp[F]
6	13	0.5	1985	4.308	1.63E-16	6.99E-12
6	13	1.5	3005	7.009	9.96E-17	5.00E-12
6	13	2.5	4635	21.98	3.17E-17	1.91E-12

Table A.2: BVD Parameters for Bare Slow Shear LFEs.

Diopter	Diameter [mm]	Separation [mm]	Rm[Ω]	Lm[H]	Cm[F]	Cp[F]
2	9	0.5	1776	38.27	1.81E-17	6.85E-13
2	9	1.5	2168	14.18	4.89E-17	1.85E-12
2	9	2.5	3610	7.77	8.92E-17	3.85E-12
2	11	0.5	1548	83.33	8.32E-18	3.14E-13
2	11	1.5	2037	8.606	8.06E-17	3.48E-12
2	11	2.5	3012	21.42	3.24E-17	1.40E-12
2	13	0.5	1639	19.42	3.57E-17	1.35E-12
2	13	1.5	2037	6.244	1.11E-16	4.80E-12
2	13	2.5	2814	11.74	5.91E-17	2.98E-12
3	9	0.5	2319	45.29	1.53E-17	6.61E-13
3	9	1.5	3056	8.767	7.90E-17	3.98E-12
3	9	2.5	4554	14.04	4.94E-17	2.98E-12
3	11	0.5	2335	59.78	1.16E-17	5.01E-13
3	11	1.5	2843	8.088	8.57E-17	4.32E-12

Diopter	Diameter [mm]	Separation [mm]	Rm[Ω]	Lm[H]	Cm[F]	Cp[F]
3	11	2.5	4632	14.77	4.69E-17	2.84E-12
3	13	0.5	2523	35.7	1.94E-17	9.78E-13
3	13	1.5	3407	962.3	7.20E-19	3.63E-14
3	13	2.5	4613	13.03	5.32E-17	3.22E-12
4	9	0.5	1840	3.574	1.94E-16	7.33E-12
4	9	1.5	2278	12.71	5.46E-17	2.36E-12
4	9	2.5	3860	14.94	4.65E-17	2.81E-12
4	11	0.5	1648	45.74	1.52E-17	6.55E-13
4	11	1.5	2655	5.994	1.16E-16	5.00E-12
4	11	2.5	3775	17.35	4.00E-17	2.42E-12
4	13	0.5	1687	8.185	8.48E-17	3.66E-12
4	13	1.5	2410	11.7	5.93E-17	2.99E-12
4	13	2.5	4292	10.6	6.54E-17	3.95E-12
5	9	0.5	1928	23.8	2.93E-17	1.47E-12
5	9	1.5	3222	1306	5.33E-19	2.68E-14
5	9	2.5	5183	20.34	3.42E-17	2.07E-12
5	11	0.5	2119	24.21	2.88E-17	1.24E-12
5	11	1.5	3320	7.225	9.63E-17	4.84E-12
5	11	2.5	4964	13.25	5.26E-17	3.17E-12
5	13	0.5	2382	25.51	2.73E-17	1.37E-12
5	13	1.5	3069	17.77	3.92E-17	1.97E-12
5	13	2.5	4895	15.99	4.35E-17	3.28E-12
6	9	0.5	2150	17.27	4.03E-17	1.52E-12

Diopter	Diameter [mm]	Separation [mm]	Rm[Ω]	Lm[H]	Cm[F]	Cp[F]
6	9	1.5	3085	7.559	9.21E-17	3.97E-12
6	9	2.5	5591	18.95	3.67E-17	1.85E-12
6	11	0.5	2007	13.8	5.04E-17	2.17E-12
6	11	1.5	3151	9.127	7.63E-17	3.83E-12
6	11	2.5	5793	12.06	5.77E-17	2.90E-12
6	13	0.5	2336	28.37	2.45E-17	1.06E-12
6	13	1.5	3128	16.38	4.25E-17	1.83E-12
6	13	2.5	5502	12.94	5.38E-17	3.25E-12

Table A.3: BVD Parameters for Fast Slow Shear LFEs.

Diopter	Diameter [mm]	Separation [mm]	Rm[Ω]	Lm[H]	Cm[F]	Cp[F]
2	9	0.5	1336	4.091	1.31E-16	5.00E-12
2	9	1.5	2096	4.389	1.22E-16	4.66E-12
2	9	2.5	2350	23.01	2.32E-17	1.33E-12
2	11	0.5	1334	5.869	9.10E-17	3.92E-12
2	11	1.5	1774	3.324	1.61E-16	6.92E-12
2	11	2.5	2370	6.047	8.83E-17	4.35E-12
2	13	0.5	1351	39.89	1.34E-17	5.76E-13
2	13	1.5	1690	32.6	1.64E-17	7.05E-13
2	13	2.5	2473	7.825	6.83E-17	3.92E-12

Diopter	Diameter [mm]	Separation [mm]	Rm[Ω]	Lm[H]	Cm[F]	Cp[F]
3	9	0.5	1609	3.109	1.72E-16	7.39E-12
3	9	1.5	1903	37.89	1.41E-17	6.07E-13
3	9	2.5	2688	29.35	1.82E-17	1.04E-12
3	11	0.5	1537	3.269	1.63E-16	7.03E-12
3	11	1.5	1741	23.57	2.27E-17	1.11E-12
3	11	2.5	2726	8.069	6.62E-17	3.80E-12
3	13	0.5	1446	46.22	1.16E-17	5.68E-13
3	13	1.5	1946	9.313	5.73E-17	2.82E-12
3	13	2.5	2937	118.4	4.51E-18	2.59E-13
4	9	0.5	1563	3.64	1.47E-16	6.32E-12
4	9	1.5	2154	4.352	1.23E-16	5.28E-12
4	9	2.5	3356	7.456	7.17E-17	4.11E-12
4	11	0.5	1579	3.428	1.56E-16	6.71E-12
4	11	1.5	1999	15.91	3.36E-17	1.65E-12
4	11	2.5	3111	12.05	4.44E-17	3.05E-12
4	13	0.5	1800	3.327	1.61E-16	6.91E-12
4	13	1.5	2283	6.665	8.02E-17	3.94E-12
4	13	2.5	3495	11.49	4.65E-17	2.67E-12
5	9	0.5	2481	19.39	2.77E-17	1.58E-12
5	9	1.5	3686	7.649	7.01E-17	4.02E-12
5	9	2.5	5341	13.54	3.96E-17	3.40E-12
5	11	0.5	2685	5.903	9.08E-17	5.20E-12
5	11	1.5	3206	15.78	3.40E-17	1.95E-12

Diopter	Diameter [mm]	Separation [mm]	Rm[Ω]	Lm[H]	Cm[F]	Cp[F]
5	11	2.5	4831	22.42	2.39E-17	1.64E-12
5	13	0.5	2782	59.59	9.00E-18	5.15E-13
5	13	1.5	4349	12.73	4.21E-17	2.41E-12
5	13	2.5	6343	12.37	4.33E-17	2.98E-12
6	9	0.5	2088	8.58	6.25E-17	3.07E-12
6	9	1.5	3202	64.96	8.25E-18	4.05E-13
6	9	2.5	5658	14.05	3.81E-17	2.62E-12
6	11	0.5	2128	8.382	6.40E-17	3.14E-12
6	11	1.5	3080	11.87	4.52E-17	2.22E-12
6	11	2.5	5725	10	5.36E-17	3.07E-12
6	13	0.5	2271	53.71	9.98E-18	4.90E-13
6	13	1.5	3635	29.28	1.83E-17	1.05E-12
6	13	2.5	5910	18.86	2.84E-17	1.63E-12

APPENDIX

APPENDIX B: MEASURED BVD PARAMETERS[8]

Characterization Technique			Advantages	Limitations
Impedance Analysis	Conventional Impedance Analyzers		• Highest accuracy. • Supports complete sensor characterization and harmonic overtones analysis. • Isolated QCM measurements. • Adequate for all mediums, provided that appropriate resolution is supported.	• Highest setup cost. • Large physical size. • Some models require time consuming processing/data fitting for accurate parameters extraction.
	Compact Circuitry	VD Based	• Significantly cheaper than conventional analyzers with more compact sizing. • Provides essential characterization parameters for different applications (e.g., BVD parameters from [4,80]).	• Less accurate compared to conventional analyzers. • Sensor is not measured in isolation (part of a circuit). • Requires time consuming processing algorithms. • Some circuits provide limited characterization [38].
		Compact Analyzers	• Maintains most conventional impedance analyzers advantages. • Rapid and high-resolution measurements capability [72]. • Low cost and high integration capability (handheld size).	• Less accurate compared to conventional impedance analyzers.
Oscillator Circuits	QCM Oscillators		• Highly integrated low cost circuitry. • Good accuracy. • Direct frequency measurement. • Dissipation monitoring capability for some designs.	• Sensor response is influenced by circuit components. • Inadequate for overtones study. • Requires high components stability. • $f_{osc} \neq MSRF$ without C_o^* compensation in-liquid.
	PLL Based	0-Phase Tracking	• Maintains QCM oscillators advantages. • Locks in to $MSRF$. • Supports simultaneous interrogation by different overtones for extended results. • Provides dissipation monitoring capability through signals indicating R_m variations.	• Requires C_o^* compensation for $MSRF$ tracking. • Circuit components influence may affect the tracking accuracy.
		G_{max} Tracking		• Requires high-resolution VCO for flat conductance peaks. • Circuit components influence may affect the tracking accuracy.
Exponential Decay (QCM-D)	Conventional		• Accurately measures series and parallel resonance. • Simultaneous f and D tracking capability and overtones excitation.	• Fairly expensive due to its high-quality components. • Mainly suitable for lab-based applications (i.e., low portability).
	Contactless		• Maintains most conventional QCM-D advantages. • Extends the applications spectrum to closed volumes (i.e., no QCM wiring). • Electrodeless setup increases the measuring sensitivity.	• Contactless setup in [114] is limited for lightly-loaded applications. • The wireless interrogation distance is still fairly low for various applications.
	Phase-Mass Characterization		• Achieves higher sensitivity and resolution compared to conventional circuitry. • Supports high-frequency crystals characterization with minimized signals noise and interference. • Highly integrated setup, supporting sensing arrays.	• Current setup provides partial sensor characterization (e.g., limited dissipation monitoring). • Limiting the applications spectrum.

BIOGRAPHY OF THE AUTHOR

Thomas "TJ" J. Leighton grew up in Brewer, Maine, the son of Thomas Leighton and Deborah Leighton, and brother of Ellie Leighton. He attended Brewer High School and graduated in 2013. TJ would continue on to enroll at the University of Maine and graduate with his Bachelor of Science in Electrical Engineering with Honors in the spring of 2017, completing his Honors thesis on the identity and motivation of upper class engineering students. After graduation, TJ accepted a position as a Graduate Teaching Assistant at the University of Maine, and attended graduate school full time starting the fall of 2017. TJ has accepted a full-time position as a Field Applications Engineer at Texas Instruments. Thomas J. Leighton is a candidate for the Master of Science degree in Electrical Engineering from the University of Maine in May 2019.